Universitat Autònoma de Barcelona

Mechanical Resonators Based on Graphene and Carbon Nanotubes

Ioannis Tsioutsios

Mechanical Resonators Based on Graphene and Carbon Nanotubes

Thesis by
Ioannis Tsioutsios

June 2016

Doctoral school in Physics, Universitat Autònoma de Barcelona (UAB)
ICFO - The Institute of Photonic Sciences

Supervisor: Prof. Dr. Adrian Bachtold
Tutor: Prof. Dr. Jordi Pascual Gainza

Thesis committee:
Prof. Dr. Francisco Javier Tamayo de Miguel
Prof. Dr. Jean-Philippe Poizat
Prof. Dr. Romain Quidant

ICFO
Institut de Ciències Fotòniques

UAB
Universitat Autònoma de Barcelona

Acknowledgments

The successful completion of my doctorate would not have been possible without the support of many people. I would like to thank them all.

First, I would like to thank my advisor **Prof. Adrian Bachtold** for giving me the opportunity to work in a scientifically motivating and highly productive environment. He was always open in new ideas and gave me the freedom to satisfy my scientific curiosity by working in multiple different projects. He always supported me and successfully guided me throughout my studies. He was always available at any moment to help me and answer my questions without any reservation. At the later stage of my doctorate, he supported me by providing the necessary independence, while keeping a continuous interest in my work and guiding it with his experience in the right direction. I also benefited from his generous support of my participation in national and international conferences, where I could present our work and exchange ideas with experts in the field.

I also thank my thesis tutor **Prof. Jordi Pascual Gainza** for all of his help and support. His availability and advice throughout the years of my Ph.D. as well as his help in administrative issues were invaluable.

I would like to thank **Prof. Francisco Javier Tamayo de Miguel**, **Prof. Jean-Philippe Poizat** and **Prof. Romain Quidant** for agreeing to serve as experts in my thesis committee. I would also like to thank **Prof. Morgan Mitchell** and **Dr. Robert Sewell** for agreeing to serve as substitute members.

When I started my Ph.D. studies, **Prof. Joel Moser** was working as a postdoctoral researcher in our group. I was very lucky that he was the person to introduce me to the nanofabrication and experimental physics techniques. Learning from his expertise, I had the chance to start my Ph.D. in strong foundations; this was crucial for the rest of my studies as well as for our work in coupled graphene resonators. He was always eager to help and assist in any problem of technical or theoretical nature I had, and I strongly benefited from his deep understanding in physics. I would like to thank him for his continuous support and guidance.

I was also very fortunate to collaborate with **Prof. Pierre Verlot** in studying the Brownian motion of carbon nanotubes. I gained a lot from his exceptional experimental and theoretical background in physics, his novel ideas and willingness to share knowledge. More importantly, his deep understanding of optomechanics helped me to have a broader view of this scientific field and of physics in general. I would like to thank him for all his help and support.

When **Alexandros Tavernarakis** joined our group as a post doctoral researcher he brought not only high motivation but also new and advanced expertise in experimental physics and optomechanics. I greatly benefited from his knowledge during our work in

studying the Brownian motion of carbon nanotubes as well as in various other projects that are not presented in the thesis. He was always available to discuss and help me with any problem I had during my studies. I would like to thank him for his continues help and support.

I would like to thank **Antoine Reserbat-Plantey** and **Nicolas Morell** for our collaboration in studying carbon nanotubes mechanical resonators optically. I enjoyed Antoine's positive attitude and his eagerness to help and share his knowledge. When Nicolas joined our team as a new master student he brought not only fresh motivation and energy, but also a lot of scientific curiosity and knowledge. I enjoyed a lot working with both of them.

I greatly enjoyed the few chances that I had to work together with **Peter Weber**. His motivation, positive attitude and critical thinking as a Ph.D student, was always a driving force for me that greatly helped me to improve and get better. I thank him for being always available to help and support me. I also thank him for his detailed and comprehensive comments on the thesis.

Working on the development of the graphene transfer technique and setup with **Johannes Güttinger** was a very exciting and productive process. His analytical thinking and organizing skills greatly contributed to this work as well as on my improvement as a scientist.

There are several other people with whom I have collaborated and who contributed to this work all the past years of my studies. I would like to thank **Alexander Eichler** for having introduced me to the ultra high vacuum setup and for helping me and answering all my questions when I was a young Ph.D student. I enjoyed a lot working with **Jil Schwender** on high frequency graphene resonators for mass sensing experiments project, the results of which are not presented in the thesis. I greatly enjoyed working with **Marko Spasenović** in coupling the motion of graphene resonators to the localised surface plasmons of gold nanoparticles and I thank him for his support and willingness to share his knowledge. I would like to thank **Dr. Jose Antonio Plaza** for performing the finite element simulation of coupled graphene resonators and his important feedback. Special thanks to **Prof. Maria Jose Esplandiu** for sharing her knowledge in nanofabrication processes and especially in carbon nanotubes growth, as well as for her continues support and help. I enjoyed a lot working with **Marianna Sledzinska** in developing high mobility suspended graphene devices and I thank her for sharing her knowledge and expertise. I thank **Bryce Kobrin** for undertaking the challenge to proof read a big part my thesis and correcting my english. I also thank **Johann Osmond** for his support on the SEM system and our fruitful discussions on nanofabrication processes. I would also like to thank the present and past members of our group, **Julien Chaste**, **Ali Afshar Farniya**, **Adrien Noury**, **Simon Hurand**, **Jorge Vergara**, **Sergio de Bonis**, for creating a nice atmosphere and a welcome social environment in our group. I greatly thank **Prof. Jordi Mompart Penina** and **Francesc Poblet**, from the physics department of UAB, for their help and support with any administrative issue I had throughout the years of my studies. Finally, I would like to thank all the people from the various workshops and departments of both ICN and ICFO, for their constant help and support.

Abstract

Mechanical resonators based on graphene and carbon nanotubes have recently attracted considerable attention, due to the great wealth of remarkable properties that they exhibit. Their intrinsically low-dimensional nature qualify them as ideal systems to study mechanics at the nano-scale. Their mass is so low that they are extremely sensitive to external forces and attached mass, which holds promise for sensing applications. In addition, these systems can vibrate at the GHz regime while their resonant frequencies can be widely tunable. Moreover, they exhibit strong mechanical nonlinearities and among their intriguing properties is the efficient coupling of their mechanical vibrations to electrons in the Coulomb blockade and Quantum Hall regimes.

However, working with these devices requires high level of control over the nanofabrication technologies as well as efficient readout and control of their motion. In this Ph.D thesis we address these requirements by fabricating and investigating various nanomechanical resonators based on graphene and carbon nanotubes, while exploring different techniques for the transduction of their motion.

We firstly study coupled mechanical resonators based on graphene and carbon nanotubes. We succeed to push the limits of modern nanofabrication techniques by realizing complex fully suspended structures that consist of two graphene membranes coupled by a multi-wall carbon nanotube. We employ electrical mixing transduction techniques to extensively characterize the complex vibrational dynamics of these systems at cryogenic temperature. Interestingly, we observe nonlinear coupling between the eigenmodes of the structures, highlighting the crucial role of nonlinearities in such nano-scale systems.

We then investigate the noise dynamics of singly-clamped carbon nanotube resonators, at room temperature, with very high sensitivity, by coupling their motion to the focused electron beam of a scanning electron microscope. This transduction scheme enables us to detect their motion in real-time and present a detailed analysis of the two-dimensional noise trajectories both in space and time. We show that these tiny objects behave as Brownian particles evolving in a two-dimensional harmonic potential. Moreover, we demonstrate phase-coherent measurements by implementing a phase-locked loop that allows us to track their resonant frequency in real-time, paving the way for high performance sensing applications.

Finally, we present the first steps towards studying suspended singly-walled doubly-clamped carbon nanotube resonators as hybrid nano-optomechanical systems, where the optical degrees of freedom are embedded inside the nanotube's structure. We develop a low temperature micro-photoluminescence setup to investigate the coupling between the mechanical vibrational modes and the localized zero-dimension excitons of the nanotubes. Additionally, we develop a chemical vapor deposition growth process for up to 10 μm long,

narrow diameter, suspended nanotubes.

Abstracto

Los resonadores mecánicos basados en grafeno y nanotubos de carbono han atraído recientemente una considerable atención, debido a la gran variedad de propiedades extraordinarias que exhiben. La reducida dimensión intrínseca a su naturaleza hace de estos materiales candidatos ideales para el estudio de la mecánica en la nano-escala. Su reducida masa les hace extremadamente sensibles a fuerzas externas y masas adsorbidas, lo cual es prometedor para su uso como sensores. A ello se suma que estos sistemas pueden ajustar ampliamente su frecuencia de vibración llegando hasta GHz. Además, muestran fuertes efectos no lineales y entre sus interesantes propiedades está el eficiente acoplamiento de sus vibraciones mecánicas con los electrones en los regímenes de bloqueo de Coulomb y de efecto Hall cuántico.

Sin embargo, trabajar con estos dispositivos requiere un alto nivel de control de las técnicas de nano-fabricación así como de una eficiente lectura y control de su movimiento. En esta tesis abordamos estos requisitos fabricando e investigando diversos nano-resonadores mecánicos basados en grafeno y nanotubos de carbono, mientras exploramos diferentes técnicas para la transducción de su movimiento.

Primero estudiamos resonadores mecánicos acoplados basados en grafeno y nanotubos de carbono. Logramos superar los límites de las técnicas de nano-fabricación modernas creando estructuras completamente suspendidas consistentes en dos membranas de grafeno unidas por un nanotubo de carbono multi-capa. Utilizamos técnicas de demodulación de corrientes eléctricas como transducción para caracterizar la compleja dinámica de las vibraciones en estos sistemas a temperatura criogénica. Observamos, de manera interesante, acoplamiento entre los modos principales de vibración de las diferentes estructuras, resaltando la importancia de las no linealidades en estos sistemas en la nano-escala.

Más tarde, investigamos la dinámica del ruido de resonadores basados en nanotubos de carbono fijados en uno de sus extremos, a temperatura ambiente, con una gran sensibilidad, acoplando su movimiento al foco de un rayo de electrones de un microscopio de electrones. Este esquema de transducción nos permite detectar su movimiento en tiempo real y presentar un análisis detallado de la trayectoria dos-dimensional del ruido en espacio y tiempo. Aquí mostramos que estos diminutos objetos se comportan como partículas Brownianas moviéndose en un potencial harmónico de dos dimensiones. Además, demostramos medidas coherentes en fase implementando un lazo de seguimiento de fase (PLL) que permite monitorizar la frecuencia de resonancia en tiempo real, abriendo el camino a aplicaciones como sensores de alto rendimiento.

Finalmente, presentamos los primeros pasos hacia el estudio de resonadores basados en nanotubos de carbono mono-capa, suspendidos y anclados en ambos extremos como sistemas híbridos nano-optomecanicos, en los cuales el grado de libertad óptico está

integrado dentro de la estructura del nanotubo. Hemos desarrollado un equipo de microfotoluminiscencia a baja temperatura para investigar el acoplamiento entre los modos de vibración mecánicos y los excitones localizados de cero dimensiones de los nanotubos. También, hemos desarrollado un proceso de deposición química de vapor (CVD) para hacer crecer nanotubos de carbono suspendidos, de hasta diez micras de longitud y diámetro reducido.

Contents

Chapter 1

Introduction

1.1 Introduction to nanotechnology

Nanotechnology is science, engineering, and technology conducted at the nanoscale. In other words it is all about understanding, controlling, and manipulating objects or materials with dimensions up to few hundreds of nanometers.

Back in December 1959, at an American Physical Society meeting at the California Institute of Technology (CalTech), Richard Feynman gave a visionary talk entitled *"There's Plenty of Room at the Bottom"*, defining the ideas and concepts behind nanotechnology and nanoscience, long before these terms were actually used. In his talk, Feynman described a process in which scientists would be able to manipulate and control individual atoms and molecules. Over a decade later, in 1974, Norio Taniguchi coined the term nanotechnology to describe semiconductor processes such as thin film deposition and ion beam milling exhibiting characteristic control on the order of a nanometer. It wasn't until 1981 though, after the development of the scanning tunneling microscope which could *"see"* individual atoms, that modern nanotechnology began.

Nowadays, more than 50 years after the famous Feynman's talk, a broad spectrum of scientific and technological fields of nanoscience and nanotechnology are very well established. Techniques like electron-beam and ion-beam lithography, molecular-beam epitaxy, nano-imprint lithography, atomic force microscopy (AFM), scanning electron microscopy (SEM), atom-by-atom manipulation, allow scientists to control and study mater at a scale of 10^{-9} meters. From the fundamental science point of view, these developments have led to systems that are so small that even quantum mechanics starts to play an important role. From a technological point of view, nanotechnology has pushed industry to produce innovative systems with complex structures and functionality, in a very small area. A typical example is a computer chip, such as the one illustrated in Figure 1.1(a), where 4.2 billions of transistors with channel length of 22 nm are interconnected and packed in an area of no more than 650 mm^2.

Nanoelectronics was arguably the field of nanotechnology that demonstrated the highest advancements in the recent years, pushing forward fabrication techniques from micrometer scales to deep sub-micron. Nonetheless, we are only at the very beginning of Feyman's vision of assembling complex multifunctional multicomponent systems, atom by atom, utilizing not only electrical but also optical an mechanical properties of nature. In this direction, other new nanotechnology fields have emerged in recent years, like

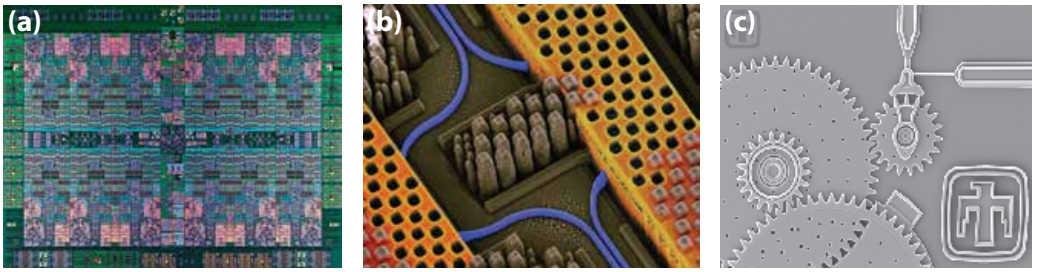

Figure 1.1: Examples from various fields of nanotechnology and nanoscience. **(a)** Image of IBM Power8 processor that consist of 4.5 billion transistors occuping an area of just 650 mm^2. **(b)** False color scanning electron microscope image of an IBM chip showing blue optical waveguides transmitting high-speed optical signals and yellow copper wires curring high-speed electrical signals. **(c)** Multiple gear speed reduction unit nanomechanical system fabricated at Sandia national laboratories.

nanophotonics (see Figure 1.1(b)) or nanomechanics (Figure 1.1(c)). The latter consists the topic of this Ph.D thesis.

1.2 Nanomechanical resonators

Nanomechanics is the scientific field of creating and controlling the motion of nano-scale objects. This field emerged as a natural evolution from Micro-Electro-Mechanical systems (MEMS), as nanofabrication techniques allowed the transition to nanometer scale of precision.

One of the types of micro- nanomechanical systems that have attracted considerable scientific and technological attention are the resonant nanomechanical systems or simply nanomechanical resonators [1]. A mechanical resonator is the mechanical manifestation and the most intuitive realization of the simple physics textbook example of a harmonic oscillator, one of the very common phenomena observed in nature, and has been an object of scientific research throughout history. One of the first scientists that systematically study them was Robert Hooke, who published a book with the basic principals of elasticity in 1676 [1, 2]. Another famous example is the Foucault pendulum which was used by Léon Foucault in 1851 for the first simple proof of earth's rotation. Nowadays, mechanical resonators have been used in a variety of fields both in science and technology, ranging from micron-scale cantilevers used in atomic-force microscopy, to meter-scale mechanical oscillators in the form of interferometer mirrors intended for probing gravitational waves.

During the last decades, there has been an increasing scientific and technological interest in the miniaturization of mechanical resonators, initially in micron-meter scales, driven by the MEMS field, and more recently in nanometer scales. Their dimensions and mass reduction, naturally leads to higher sensitivity to external forces that are acting on them, making nano-scale resonators very interesting systems for mass, charge, and

[1] Resonator is a system that exhibits resonant behavior, that is, it naturally oscillates at some frequencies with greater amplitude than at other. These frequencies are called resonant frequencies. A physical system can have as many resonant frequencies as it has degrees of freedom; each degree of freedom can vibrate as a harmonic oscillator.

force sensing experiments and applications ([3, 4, 5, 6]). Furthermore, there is an increasing technological necessity for integrating systems in small dimensions, like on-chip nanomechanical resonators for RF signal filtering, sensing or frequency reference. From the fundamental research point of view, nanomechanical resonators have been used for observing quantum phenomena at a macro-scale [2], allowing the detection of their zero-point fluctuations [7, 8, 9], the demonstration of quantum backaction noise [10], or the creation of non-classical optomechanical states [11].

1.3 Top-down versus bottom-up fabrication approaches

There are mainly two different approaches that researchers and engineers follow to fabricate these nanoscale mechanical resonators, the *top-down* and the *bottom-up*. Top-down approach is the most broadly used and the one that is predominately used for large scaled integrated systems, such as the computer chip previously illustrated in Figure 1.1(a). The basic concept is the following: the process starts from bulk material and after a sequence of lithographic patterning steps and other nanofabrication techniques, it is patterned into functional elements which could be for example transistors, waveguides, solar cells or mechanical systems. In other words, it is a process of sculpting a bulk material into a functional shape. In Figure 1.2(a-c) examples of nanoresonators that have been fabricated with top-down approach are illustrated. The geometries vary from doubly-clamped nanobeams (Figure 1.2(a)) to cantilevers (Figure 1.2(b)) or examples of even more complicated structures like coupled nanobeams (Figure 1.2(c)).

The advantage of top-down approach relies on that most of the processes are based on the very well established and mature CMOS processes. At the same time, it enables easy large scale integration by patterning several structures in parallel on the same bulk material. Nonetheless, few important short-comings exist. Firstly, there is a natural limit on the highest achievable lithographic resolution and the smallest possible feature size. Moreover, all the physical and chemical processes, which are taking place to give shape on a device, introduce defects on the surface. As the devices are getting smaller and smaller, the relative amount of these defects is increasing. Consequently, below a certain size limit, the electrical, optical, and mechanical properties of the materials begins to degrade, which imposes limitions on the minimum size of these structures.

However, in recent years there have been an increasing scientific interest in using bottom-up nanofabrication techniques for the implementation and studying of nanomechanical systems. The bottom-up approach starts with intrinsically nanoscale materials and builds them up into functional nanodevices. While this approach is less suitable for large scale integration, it demonstrates some notable advantages: The produced systems are free of defects and imperfections that characterizes the top-down fabrication methods, maintaining their intrinsic physical properties at the nanoscale. Among the various nanoscale materials, graphene and carbon nanotubes are especially promising.

[2] Nanomechanical resonators are very small but still orders of magnitude bigger than single molecules. Thus, can be considered as a macro-scale object in comparison to single atoms.

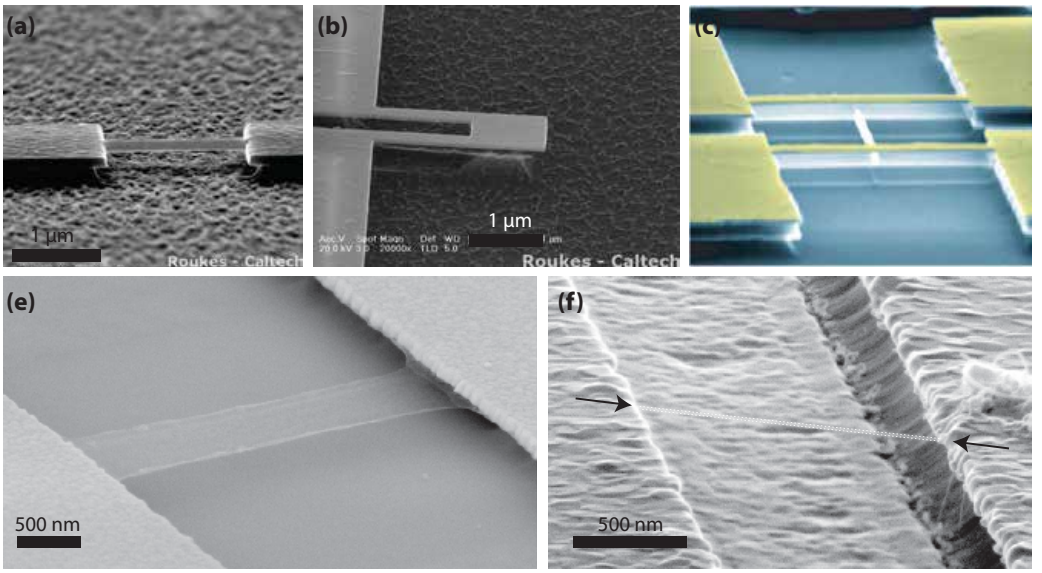

Figure 1.2: Examples of various nanomechanical resonators. **(a)** Scanning electron microscope image of a doubly-clamped, top-down fabricated, silicon carbide with aluminum on top mechanical resonator, from Roukes group at Caltech. **(b)** Scanning electron microscope image of a nanocantilever made out of a 100 nm silicon nitride membrane, from Roukes group at Caltech. **(c)** Scanning electron microscope image of silicon based doubly-clamped coupled nanoresonators [12]. **(e,f)** Scanning electron microscope images of doubly clamped graphene and carbon nanotube resonators [13].

1.4 Graphene and carbon nanotube mechanical resonators

Mechanical resonators based on graphene and carbon nanotubes have recently attracted considerably attention. Graphene is a truly two-dimensional (2D) crystal of carbon atoms and carbon nanotube is its one-dimensional (1D) counterpart. A typical example of such systems in doubly-clamped configuration is illustrated in Figure 1.2(e,f), while other configurations like drums-shaped graphene or singly-clamped nanotubes are also common.

The high strength, low mass, and high chemical stability of these materials, combined with their also exceptional electrical properties, allows for the realization mechanical resonators with outstanding performance[3]. Their mechanical resonant frequencies can reach the GHz regime [14, 15], their quality factor can be very high [16, 13, 17], and their resonant frequency exhibit extremely high tunability [18, 19]. Moreover, these systems can be used as sensors of mass [20, 21] and force [22, 23] with unprecedented sensitivity.

Apart from their high performance, the most fascinating aspect these systems is that they represent the ultimate one-dimensional and two-dimensional limit that can be found in nature. Studying nanomechanics in this regime could lead to new unexpected phenomena and novel systems with unique proprieties. Interesting properties like the effi-

[3]More detailed information on the graphene and carbon nanotubes structure and properties will be given in chapter 2.

cient coupling of their mechanical vibrations to electrons in the Coulomb blockade and the quantum Hall regimes [24, 25, 26, 27, 28] or their strong mechanical nonlinearities [13, 29, 30] qualify graphene and carbon nanotube resonators as very intriguing systems to investigate nanomechanics at the ultimate scaling limit.

1.5 Thesis motivation and outline

While mechanical resonators based on graphene and carbon nanotubes exhibit a breadth of remarkable properties, the full exploitation of their potential inevitably requires further investigation on the nanofabrication and motion transduction schemes.

In this direction, the present Ph.D thesis targets on exploring nanomechanics at the extreme scaling limit of these one- and two-dimensional mechanical resonators. One the hand, by improving nanofabrication technologies, and on the other hand, by exploring the detection sensitivity limits, utilizing and optimizing various transduction schemes. To do so, I worked in various experiments using different experimental techniques. In this manuscript I describe the results of the three main experiments I worked on during my Ph.D studies. An outline is given below:

- Chapter 2 gives a brief introduction on the electrical, optical, and mechanical properties of graphene and carbon nanotubes.
- Chapter 3 gives a brief introduction on the main theoretical concepts that are necessary to understand the basic dynamical properties of nanomechanical resonators.
- Chapter 4 briefly describes the various transduction schemes that exist for graphene and carbon nanotube resonators.
- Chapter 5 describes the development, fabrication and characterization of coupled graphene mechanical resonators, where we observed nonlinear coupling between the eigenmodes in these systems.
- Chapter 6 presents our study on the Brownian motion of carbon nanotubes in real time, at room temperature, using a focused electron beam of a scanning electron microscope.
- Chapter 7 presents the first steps towards studying suspended single-walled carbon nanotubes as hybrid nanomechanical resonators, by investigating the coupling between the energy level of localized excitons and the mechanical degrees of freedom of the nanotubes. For this purpose we developed a low temperature microphotoluminescence setup.

Chapter 2

Graphene and carbon nanotube properties

In this chapter we will give an overview on the physical properties of graphene and carbon nanotubes. In the first section we will give a brief introduction to the history of these materials. We will then describe their properties as defined from their unique crystallographic structure, starting from their electronic properties, continuing with their optical properties, and ending with their mechanical properties. If necessary, additional information will be given in each chapter separately.

2.1 Introduction

Graphene is an atomic-layer of covalently bonded carbon atoms arranged into a honeycomb lattice (Figure 2.1(a)), a truly two-dimensional crystal and the very first observed in nature [31]. Remarkably, all the existing graphitic materials of all other dimensionalities have graphene as the basic building block. For instance, 0D fullerenes, such as C60 (buckyball) (Figure 2.1(b)), are essentially graphene which is wrapped up into spheres, carbon nanotubes are graphene which is rolled up into thin cylinders (Figure 2.1(c)), while bulk 3D graphite consist of many graphene layers stacked together (Figure 2.1(d)). Interestingly, for more than 70 years it was widely believed that 2D crystals are thermodynamically unstable and thus could not exist in nature [32]. It wasn't until very recently that two scientists from Manchester, thanks to their "Friday night experiments" in 2004, demonstrated that this 2D crystal can actually be isolated on top of silicon substrate [31]. Shortly afterwards it was shown that it can be also obtained in liquid [33] or as suspended membrane [34]. These developments catalyzed an enormous effort of the scientific community to study this material and other 2D crystals, rewarding the two scientists, Dr. Andre Geim and Dr. Konstantin Novoselov, the Nobel Prize in physics in 2010.

Already before the discovery of graphene, carbon nanotubes have been an object of intense research after their experimental discovery by Iijima *et al.* (1991) [35]. These one-dimensional crystals can be separated into two categories: single-walled carbon nanotubes (SWCNTs) and multi-walled carbon nanotubes (MWCNTs). SWCNTs are typically 1-2 nm in diameter and several μm in length. MWCNTs essentially consist of concentric SWNTs (or shells) stacked together. Their diameter range from 5 to 50 nm and they are

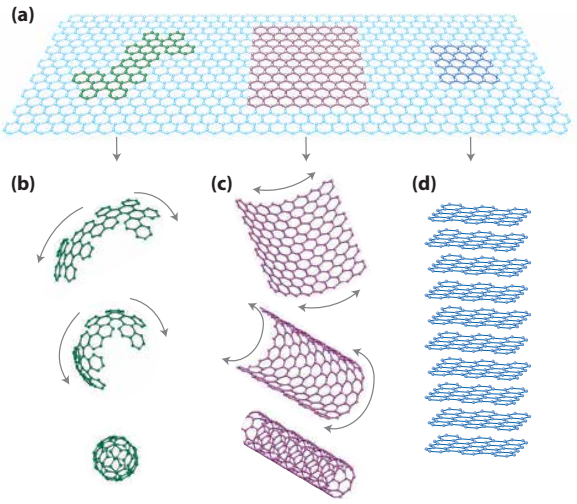

Figure 2.1: Graphene as the basic building block of all carbon materials of other dimensionalities. **(a)** Graphene 2D atomic structure. **(b)** Graphene wrapped up into 0D fullerene. **(c)** Graphene rolled into nanotube. **(d)** Graphene layers stacked in to graphite. Figure adapted from [32].

typically several tens of μm in length.

To thoroughly understand the dynamics, the interaction with the environment, and the motion transduction mechanisms of mechanical resonators based on these nano-scale materials, it is very useful to understand their physical properties, which are very much interrelated since graphene is the basic building block of carbon nanotubes. Therefore, their main electrical, optical, and mechanical properties will be briefly presented in the following sections.

2.2 Electrical properties of graphene and carbon nanotubes

The electrical properties of graphene are very much defined by its unique crystallographic structure. The $\mid 2s\rangle$ and the in-plane $\mid p_x\rangle$ and $\mid p_y\rangle$ orbitals of its carbon atoms, hybridize to form a strongly bound σ system which is called sp^2 hybridization. As a result, atoms in graphene condense in a honeycomb lattice. Three electrons per atom are involved in strong σ bonds, and one electron from the perpendicular to the graphene plane $\mid p_z\rangle$ orbital yields the π bonds. The electronic properties of graphene at low energies are defined by the π electrons, whereas σ electrons form an energy band far away from the Fermi energy.

The honeycomb network of graphene can be described as a triangular (or hexagonal) lattice with a basis of two atoms (Figure 2.2**(a)**). The primitive unit-cell spanned by these vectors is a rhombus with a side length of $a = 0.246$ nm and a carbon-carbon distance of

$a_{C-C} = 246\ \text{nm}/\sqrt{3} = 0.142\ \text{nm}$. The lattice vectors can be written as

$$a_1 = \begin{pmatrix} a \\ 0 \end{pmatrix} \quad \text{and} \quad a_2 = \begin{pmatrix} \frac{1}{2}a \\ \frac{\sqrt{3}}{2}a \end{pmatrix}, \tag{2.1}$$

and the reciprocal lattice vectors are given by

$$b_1 = \begin{pmatrix} \frac{2\pi}{a} \\ \frac{2\pi}{\sqrt{3}a} \end{pmatrix} \quad \text{and} \quad b_2 = \begin{pmatrix} 0 \\ \frac{\sqrt{4\pi}}{\sqrt{3}a} \end{pmatrix}. \tag{2.2}$$

The first Brillouin zone is constructed as the Wigner-Seitz cell of the reciprocal lattice and has the shape of a hexagon (Figure 2.2(b)). As it was mentioned earlier, the low energy electronic properties of graphene are governed by the valence $\mid p_z \rangle$ electrons. Following a tight-binding approximation on the wavefunction of these electrons, their energy dispersion in the lattice of graphene can be calculated [36, 37]. The valence band and the conduction band touch at six points, the so-called Dirac or neutrality point. For symmetry reasons, these six points can be reduced to the two inequivalent corners of the Brillouin zone, K and K' (Figure 2.2**b**). Their position is given by

$$K = \frac{2\pi}{a}\begin{pmatrix} \frac{1}{3} \\ \frac{1}{\sqrt{3}} \end{pmatrix} \quad and \quad K' = \frac{2\pi}{a}\begin{pmatrix} \frac{2}{3} \\ 0 \end{pmatrix}. \tag{2.3}$$

The energy dispersion for the valence and the conduction band is given by

$$E(\mathbf{k}) = \pm\gamma_0\sqrt{1 + 4\,cos\frac{\alpha k_x}{2}\,cos\frac{\sqrt{3}ak_y}{2} + 4\,cos^2\frac{ak_x}{2}}, \tag{2.4}$$

where $\gamma_0 = 2.8\,\text{eV}$ denotes the nearest hoping integral [37], and $k_i (i = 1, 2)$ the components of the wavevector in the x,y directions. Decisive for the understanding of graphene's electronic properties is the dispersion relation at the Dirac points in the vicinity of the Fermi energy. A linear expansion of equation (2.4) gives a quasi-linear energy dispersion around K and K'

$$E(\mathbf{k}) = \hbar u_{\text{F}}|\mathbf{k}|, \tag{2.5}$$

with constant Fermi velocity $u_{\text{F}} = \sqrt{3}a\gamma_0/2\hbar = 10^6$ m/s. As a consequence, electrons in these states behave as massless particles like relativistic Dirac Fermions. The energy band can be seen as two cones touching at E_{Dirac} (Figure 2.3), which means that graphene is a zero band-gap semiconductor. The symmetry of the band structure suggests that electrons and holes have the same properties.

Thanks to the massless behavior of electrons and the high Fermi velocity, graphene exhibits outstanding transport properties. In particular, electron mobilities of up to 10^6 cm^2/Vs have been observed at low temperatures [38, 39, 40]. In the ballistic transport regime, carriers can move with the Fermi velocity. Furthermore, graphene exhibits strong ambipolar electric field effect [31] with very high transconductance both in DC and high frequency AC electric fields [41]. In the context of nanomechanics, this property allows the use of suspended graphene sheets in transistor configuration in order to electrically read out its mechanical vibrations (see chapter 4).

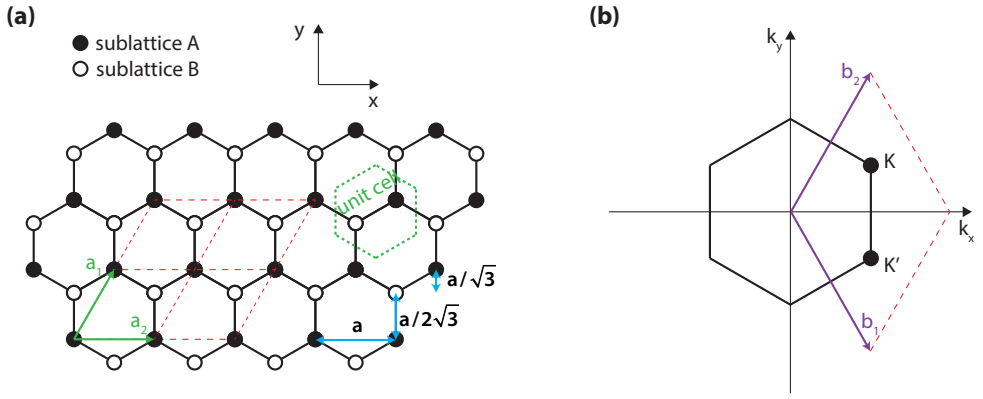

Figure 2.2: Graphene crystal lattice unit cell and Brillouin zone. **(a)** Graphene lattice with two triangular sub-lattices A and B. Each red parallelogram represents a unit cell, with side-width a = 246 nm, containing one A and one B carbon atom. **(b)** Brillouin zone of the hexagonal reciprocal space. The Dirac cones are located at the two equivalent points, K and K'.

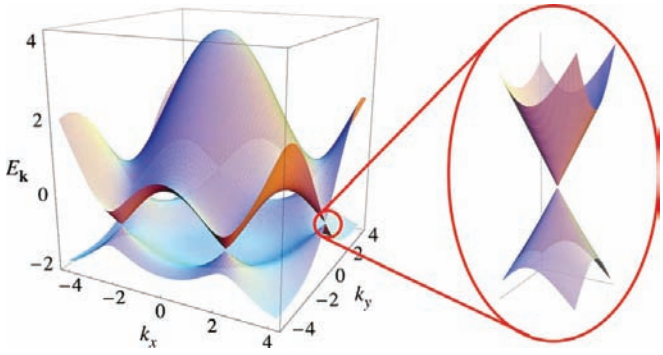

Figure 2.3: Electronic dispersion in the honeycomb lattice of graphene. Left: three-dimensional band structure of graphene. Right: zoom in of the energy bands close to one of the Dirac points. Figure adapted from [37].

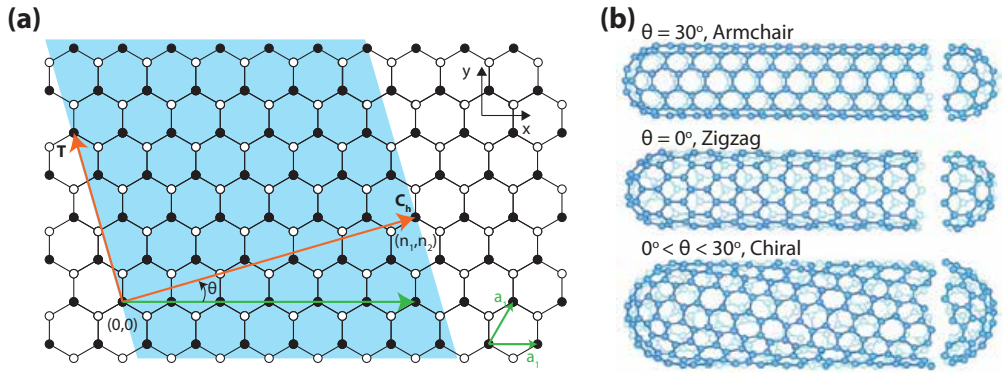

Figure 2.4: Single-walled carbon nanotube chiralities. **(a)** A particular spiece of single-walled nanotube is defined when a grpahene sheet is rolled up allong the chirality vector $\boldsymbol{C_h} = n_1\boldsymbol{a_1} + n_2\boldsymbol{a_2}$, where θ is the chiral angle, (n_1, n_2) are the chiral indices, and $\boldsymbol{T}$ the vector parallel to the nanotube's axis. **(b)** The three geometric classes of SWNTs determined by the special symmetry directions along the graphene lattice, including armchair (n, n), zigzag $(n, 0)$ and the general case chiral (n_1, n_2).

As it was mentioned earlier, single-walled carbon nanotubes can be seen as rolled up graphene. Effectively these are one-dimensional (1D) objects with axial symmetry. Depending on the different orientations of the graphene lattice with respect to the nanotube axis, which is called chirality, carbon nanotubes can exhibit different properties. The chirality vector is defined as $\boldsymbol{C_h} = n_1\boldsymbol{a_1} + n_2\boldsymbol{a_2}$ and the integer pair $(\mathrm{n_1}, \mathrm{n_2})$ uniquely determines the diameter and the chiral angle θ_C and therefore their electronic properties (Figure 2.4(a)). Moreover, they can be divided in three geometrical classes determined by the special symmetry directions along the graphene lattice, including armchair (n, n), zigzag $(\mathrm{n}, 0)$ and the general case chiral $(\mathrm{n_1}, \mathrm{n_2})$. An illustration of the different SWNT groups is given in (Figure 2.4(b)).

Following similar methodology as in the case of graphene, and by imposing the periodical boundary conditions that arise from the chirality vector, it is possible to calculate the electronic properties of single walled carbon nanotubes [42]. Impressively, depending on their chirallity, sinlge-wall carbon nanotubes could either behave as semiconductors or metals [42]. The discrimination can be achieved by evaluating $\mathrm{mod}(2n_1 + n_2, 3)$ [1]. For mod1 or mod2 the nanotube is semiconducting and mod0 is metallic (Figure 2.5). The transport of carriers occurs only along the axis of the nanotube, essentially making a CNT an 1D conductor. The bandgap energy of semiconducting nanotubes depends on their diameter and is given by $\mathrm{E_g} = 0.7$ eV/D(nm) ([43]).

Based on the exceptional transport properties of graphene, single-walled carbon nanotubes also present high electron mobility in the order of 10^4 cm^2/Vs at room temperature [44] as well as strong ambipolar field effect. Similarly to graphene resonators, these properties allow for the implementation of single-walled carbon nanotubes in a transistor configuration and electrical read out of their motion (see chapter 4).

[1] This function yields the residual of dividing $2n_1 + n_2$ by 3. We notate mod$N$ when the value of the residual is N

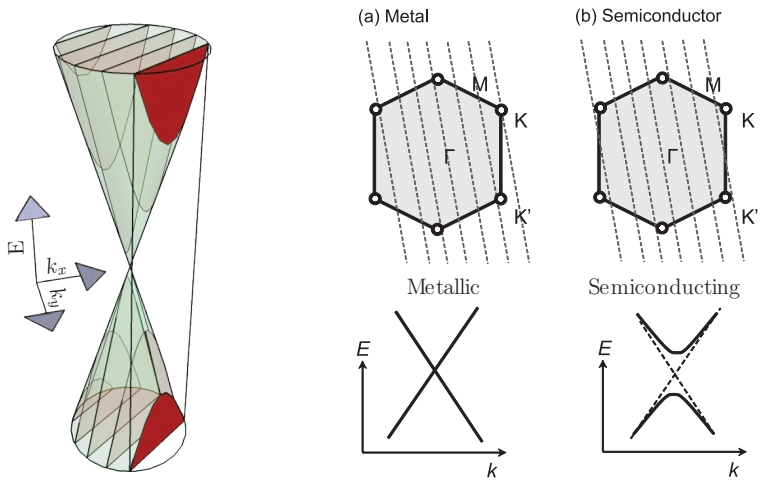

Figure 2.5: Single-walled carbon nanotube band structured inferred from graphene. Figure adapted from [45].

2.3 Optical properties of graphene and carbon nanotubes

The optical properties of graphene and carbon nanotubes are also a field of intense research for both technological and fundamental purposes. It has been predicted theoretically [46] and obtained experimentally [47] that the high-frequency (dynamic) conductivity G of graphene should be a universal constant equal to $e^2/4\hbar$. This would mean that graphene's optical transmittance T and reflectance R are also universal and given by

$$T \equiv (1 + 2\pi G/c)^{-2} = (1 + \frac{1}{2}\pi a))^{-2} \approx 0.977 \quad \text{and} \quad R \equiv \frac{1}{4}\pi^2 a^2 T, \tag{2.6}$$

for the normal light incidence, where a is the fine structure constant. Thus, a single monolayer graphene should transmit ~ 97 % of the incident light and absorb ~ 2.3 % [47, 48] (Figure 2.6), independent of its wavelength, while the reflectivity is very low (< 0.1 %). Deviations were only observed in far-IR and UV. The origin of these optical properties lies in the two-dimensional nature and zero band gap electronic spectrum of graphene. Its low absorption and reflectivity suggest that the optical readout of a nanomechanical system based on graphene is a challenging process. Nonetheless, the first experimental demonstration of graphene vibrations was achieved employing optical interferometry [22].

The rich optical properties of single-walled carbon nanotubes arise from electronic transitions within the density of states in their band structure (Figure 2.7). Although both metallic and semiconducting nanotubes allow for the investigation of Raman scattering, the observation of visible to near infrared photoluminescence (PL) is limited to semiconducting single-walled nanotubes with large enough band-gaps. Attributed to the 1D nature of carbon nanotubes, the so-called van-Hove singularities appear on the valence and conduction band edges [42]. These are illustrated in Figure 2.7), where optical transition are labeled as $E_{NN}(N = 1, 2, 3...)$. In a typical photoluminescence experiment an

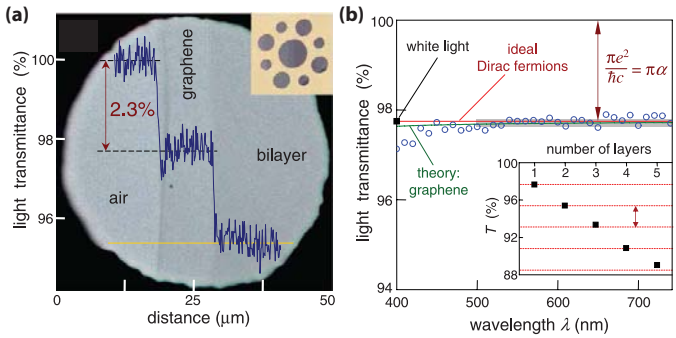

Figure 2.6: Light transmition in graphene. **(a)** Light scan profile shows the intensity transmission of white light in single layer and bilayer graphene. **(b)** Transmittance spectrum of single-layer graphene. Figure adapted from [47].

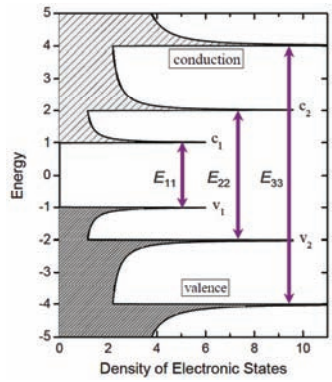

Figure 2.7: Density of states in single-walled carbon nanotubes. The so-called van-Hove singularities arise at the band edges due to the 1D nature of carbon nanotubes. The conduction and valence bands are label as c_N and v_N ($N = 1, 2, 3...$) respectively. The optical transition are denoted as E_{NN}. Figure adopted from [49].

electron hole-pair is created by optically exciting its E_{22} or E_{33} transition. Through various decay mechanisms eventually light is emitted from its E_{11} transition. Interestingly, the optical transition energies depend on the chirality of each nanotube. As a result, a resonant excitation of the E_{22} transition together with the E_{11} emission is a fingerprint of a given nanotube specie.

2.4 Mechanical properties of graphene and carbon nanotubes

The mechanical properties of graphene and carbon nanotubes are no less interesting compared to their electronic or optical properties. Due to the high strength of the hybridized sp^2 bonds between carbon atoms, their intrinsic strength exceeds this of any other ma-

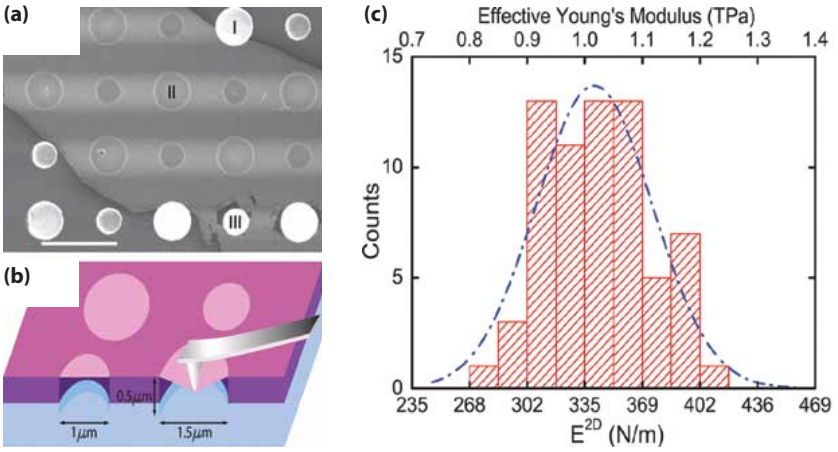

Figure 2.8: Lee *et al.* (2008) [55] measured the stiffness of grpahene using an AFM tip. **(a)** Scanning electron microscopy image of a graphene flake spanning an array of circular holes of $1 - 1.5\ \mu m$ diameter. **(b)** Schematic of nanointentation on suspended graphene membrane. **(c)** Histogram of measured elastic stiffness. Figure adapted from [55].

terial [50]. Combined with their very low mass density[2] and high chemical stability, graphene and carbon nanotubes qualify as ideal materials for implementing nanomechanical systems.

The experimental investigation of the mechanical properties of these materials, like the Young's modulus E, the Poisson ration ν, the breaking strength σ_{int} and strain ϵ_{int}, and the bending rigidity B, is a very challenging process mainly due to their very low dimensions. Their Young's modulus is very high, $E = 1$ TPa [3], and already known indirectly from experiments done on graphite [51, 52]. As expected, the same value was later confirmed in experiments performed directly on suspended multi-walled nanotubes using an AFM tip [53], on single-walled nanotubes by measuring their transport properties[54] or mechanical vibrations [18], and on graphene using an AFM tip [55] (also see Figure 2.8). In addition to their very high Young's modulus, their breaking strength is measured to be $\sigma_{int} \sim 40$ Gpa [56, 55] which corresponds to a strain of $\epsilon_{\text{int}} \sim 0.25$ *or* 25 %, entitling them to be among the strongest materials in the world.

A very challenging to estimate property of two-dimensional materials like graphene is the bending rigidity B. Since this material is only one atom thick, this value is an intrinsic property of the material and will depend only on the interaction of π and σ bonds while bending. This will give much lower values compared to continuum mechanics calculations. According to molecular dynamics calculations, this value is estimated to be $B = 1$ eV [57].

[2]The two-dimensional mass density of graphene is $\rho_{\text{G}} = 7.7 \times 10^{-7}$ Kg/m^2 and if it is rolled up into a single-walled nanotube with a typical radius of 1.5 nm, results to a three-dimensional mass density of $\rho_{\text{CNT}} = 1350$ Kg/m^3.

[3]Assuming that the thickness of graphene is 0.34 nm, its two-dimensional Young's modulus will be 340 N/m.

Chapter 3

Nanomechanical resonators

In this chapter we will introduce the main theoretical concepts that are necessary to comprehend the basic dynamical properties of nanomechanical resonators. If necessary, depending on the studied system, additional theoretical considerations will be given in each chapter separately.

We will first introduce the simple harmonic oscillator. We will then study its response to incoherent fluctuating thermal forces and to coherent external driving force. Finally, we will discuss the duffing oscillator with and without including nonlinear damping.

3.1 Introduction

Modern micro- and nano-mechanical resonators are fabricated from a range of different materials and in various forms, such as singly-clamped cantilevers, doubly-clamped beams, drums made of 2D nanomaterials, like graphene, or other more complicate structures like arrays of coupled systems. Mechanical motion in these systems results from their intrinsic elasticity and extrinsic clamping conditions, which lead to a restoring force towards a given equilibrium position. The motion is characterized by a set of orthogonal eigenmodes each having a distinct resonance eigenfrequency and displacement shape, which are obtained by solving the characteristic elastic equations [58]. For simple geometries, such as a singly-clamped or doubly-clamped beam, analytic solutions can be found. For instance, the displacement shape of their first three flexural modes are depicted in Figure 3.1. In the case of carbon nanotubes and graphene resonators, analytical solutions can also be found by treating them as one-dimensional strings and as two-dimensional membranes respectively, while finite-element numerical simulation can be employed to identify the eigenfrequencies and eigenshapes for geometrically more complex nanoresonators.

As long as the different mechanical eigenmodes of a nanoresonator are spectrally well isolated from each other and no mode-coupling [60, 61] effects exist, the one-dimensional harmonic oscillator can be used as a prototype for each one. This allows to phenomenologically describe such systems with very few parameters, while additional terms can be added to describe more complex nonlinear phenomena. This is the approach that has been predominantly followed for the studied systems that are presented in this thesis. In the following sections we are going to develop the basic theoretical concepts and formalism.

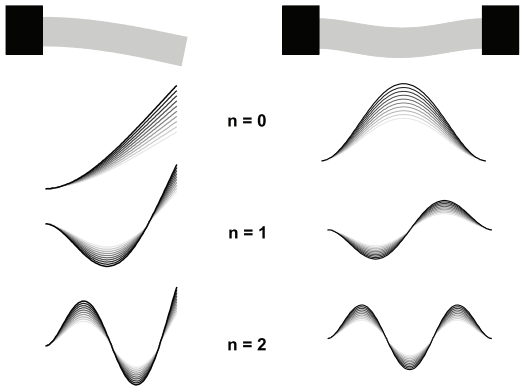

Figure 3.1: Schematic of the first three flexural modes of a singly-clamped beam (left) and a doubly clamped beam (right). Figure adapted from [59].

3.2 Harmonic oscillator

A simple harmonic mechanical oscillator without driving or damping [1] follows Hook's law

$$F = -kx(t), \tag{3.1}$$

where $x(t)$ is the displacement in time domain and k the spring constant of the system. According to Newton's second law

$$F = m_{\text{eff}} \frac{d^2x}{dt^2} = -kx(t) \Rightarrow m_{\text{eff}} \frac{d^2x}{dt^2} + kx(t) = 0, \tag{3.2}$$

where m_{eff} is the effective mass of the nanomechanical resonator. In reality, the effective mass is lower than the actual physical mass of the system, depending on the system's geometry and on the shape of each mechanical mode. The solution to the lossless equation (3.2) can be written in a complex notation as

$$x(t) = x_0 \exp(-i\omega_0 t + i\varphi), \tag{3.3}$$

where ω_0 is the mechanical angular resonance frequency of the oscillator, given by $\omega_0 = \sqrt{\frac{k}{m_{\text{eff}}}}$. The phase angle φ and amplitude x_0 are determined by the initial conditions.

So far we haven't included any interaction of the resonator's mass with the environment, like friction, noise or external driving. We can achieve this by adding a time-depended force term $F_{\text{env}}(t)$. The equation of motion will then become

$$m_{\text{eff}} \frac{d^2x}{dt^2} + kx(t) = F_{\text{env}}(t). \tag{3.4}$$

Forces which arise from the environment can be represented with two different terms in the equation of motion. The first one is the dissipation term which is typically proportional

[1] We will define and include damping on a later stage of the analysis.

to the velocity, dx/dt. The second term represents all the driving forces applied on the resonator which can be simply expressed with a time-depended force term $F(t)$. For example $F(t)$ can be a random noise force or a coherent oscillating force. Equation (3.4) can be then written as

$$m_{\text{eff}}\frac{d^2x(t)}{dt^2} + kx(t) + m_{\text{eff}}\gamma_{\text{m}}\frac{dx(t)}{dt} = F(t), \tag{3.5}$$

where the constant γ_{m} relates the linear mechanical dissipation rate to the average velocity. Both ω_0 and γ_{m} are given in radial units. To present the experimental data of this thesis, in most of the cases we will be using the ordinary frequency $f_0 = \omega_0/2\pi$, given in Hz units.

The dissipative term in (3.5), $m_{\text{eff}}\gamma_{\text{m}}\frac{dx(t)}{dt}$, is essentially the one that couples the mechanical oscillator to the environment, while γ_{m} is defining the rate of the energy exchange between them. A figure of merit to quantify this damping is the dimensionless quality factor Q, which is defined as

$$Q = 2\pi\left(\frac{Total\ energy}{Energy\ lost\ in\ one\ cycle}\right). \tag{3.6}$$

In the limit of small damping rate, $\gamma_m \ll \omega_0$, the quality factor can be approximated by $Q = \omega_0/\gamma_m$. Essentially, the quality factor gives the number of cycles that are needed for the system to loose its energy to the environment. This means that the oscillator's energy exponentially decays with a characteristic time $\omega_0\tau = 1/Q$.

Very often it is convenient to study a mechanical oscillator in the frequency domain. For this aim, we perform a Fourier transform [2] of (3.5) to obtain:

$$x(\omega) = \chi(\omega)F(\omega). \tag{3.7}$$

This expression describes the linear response of the mechanical oscillator in the frequency domain, where a force $F(\omega)$ leads to a mechanical response $x(\omega)$, which is defined by the mechanical susceptibility $\chi(\omega)$ that is given by

$$\chi(\omega) = \frac{1}{m_{\text{eff}}[\omega_0^2 - \omega^2 - i\gamma_{\text{m}}\omega]}. \tag{3.8}$$

Experimentally though, we usually do not measure the susceptibility of an oscillator directly. A common method is to record the *power spectral density* spectrum $S_{aa}(\omega)$ of a signal $a(t)$ that contains the information of the $x(t)$ trajectory. The nature of this signal depends on the motion transduction mechanism and the experimental setup [3]. *Power spectral density* essentially describes how the power of the quantity $a(t)$ is distributed in

[2] For the transform we are using the following convention $x(\omega) = \int dt\ x(t)\ e^{i\omega t}$ and $x(t) = \frac{1}{2\pi}\int d\omega\ x(\omega)\ e^{-i2\pi t}$.

[3] For instance, $a(t)$ can be the electrical signal at the output of a photodetector when the mechanical motion is detected optically, or the current that is flowing through a nanotube or graphene when their motion is detected electrically. More information on the various motion transduction techniques is given in chapter 4.

frequency space [4]. The autocorrelation function of $a(t)$ is defined as

$$C_a(\tau) = \langle a(t)a^*(t+\tau)\rangle, \tag{3.9}$$

where $\langle ...\rangle$ denotes the statistical mean. The Wiener-Khintchine theorem states that the autocorrelation function of $C_a(t)$ and the *power spectral density* $S_{aa}(\omega)$ of $a(t)$ are a Fourier transform pair [62]. This means that the *power spectral density* of $a(t)$ is given by the Fourier transform of equation (3.9)

$$S_{aa}(\omega) = \int_{-\infty}^{\infty} d(\tau)\langle a(t)a^*(t+\tau)\rangle e^{-i\omega\tau}. \tag{3.10}$$

$S_{aa}(\omega)$ is in units of $[a^2/\text{Hz}]$, where $[a]$ is the unit of the measured quantity $a(t)$ [5]. Moreover, it can be shown that the variance of the quantity $a(t)$ is the area under the one-sided *power spectral density*

$$\langle a^2\rangle = \frac{1}{2\pi}\int_0^{+\infty} d\omega S_a(\omega) = \int_0^{+\infty} df S_a(f). \tag{3.11}$$

If the Fourier transform of $a(\omega)$ is already known we can then obtain from (3.10)

$$S_{aa}(\omega) = \langle a(\omega)a(-\omega)\rangle. \tag{3.12}$$

By plugging (3.7) into (3.12) we obtain

$$S_{xx}(\omega) = |\chi(\omega)|^2 S_{FF}(\omega), \tag{3.13}$$

where $S_{FF}(\omega)$ is the *power spectral density* of the force acting on the mechanical oscillator.

Going back to equation (3.5), we can now estimate the response of a damped harmonic oscillator for driving force $F(t)$ of various origins.

3.2.1 Response to incoherent, fluctuating thermal forces

A fundamental force acting on a mechanical oscillator is the thermal force, which is a random fluctuating force $\delta F^{\text{th}}(t)$. The interaction of this force with a damped mechanical oscillator, as described by equation (3.5), will lead to its motion the so-called thermal or Brownian motion. Essentially, the thermalization process of a resonator with its environment happens due to the dissipative term, $m_{\text{eff}}\gamma_{\text{m}}\frac{dx(t)}{dt}$. This is a phenomenon that was quantitatively described for the first time by Einstein in 1905 and can be generalized through the fluctuation-dissipation theorem [63]. In thermal equilibrium, fluctuation-dissipation theorem relates the fluctuating thermal forces to the dissipative part in the equation of motion (3.5) of a mechanical oscillator. Using this theorem and by following

[4] To avoid any confusion, S_{aa} refers to double-sided power spectral density, meaning that contains information for both negative and positive frequencies around DC, while S_a refers to the single-sided and contains only the positive frequency components. It is true that $S_a(\omega > 0) = 2S_{aa}(\omega > 0)$. Practically, a typical spectrum analyzer equipment, usually records only single-sided spectra because the spectrum of a real-world signal is symmetrical around DC

[5] For instance, the experimental data recorder from a spectrum analyzer will be in units of $[\text{V}^2/\text{Hz}]$ and with the correct calibration process the data could be converted in units of actual displacement $[\text{m}^2/\text{Hz}]$.

the linear response theory [64], we get the single-side thermal force noise power spectral density

$$S_F^{\mathrm{th}}(\omega) = -\frac{4k_{\mathrm{B}}T}{\omega}\,\mathrm{Im}\Big(\frac{1}{\chi(\omega)}\Big). \tag{3.14}$$

In the weak damping limit, $\gamma_{\mathrm{m}} \ll \omega_0$, the last expression can be written as

$$S_F^{\mathrm{th}}(\omega) = 4m_{\mathrm{eff}}\gamma_{\mathrm{m}}k_{\mathrm{B}}T. \tag{3.15}$$

The thermal force spectrum is white [6] and depends on the ambient temperature of the oscillator as well as on its dissipation rate γ_{m}, while it scales with the effective mass m_{eff}. This result resembles the expression for the Johnson-Nyquist noise [65] of voltage fluctuations $\delta u(t)$ across a resistor R, $S_u = 4k_{\mathrm{B}}TR$. Both phenomena are related and can be explained with the fluctuation-dissipation theorem. The thermal *power spectral density* $S_x^{\mathrm{th}}(\omega)$ of the mechanical oscillator can be then written as

$$S_x^{\mathrm{th}}(\omega) = \frac{4\gamma_{\mathrm{m}}k_{\mathrm{B}}T}{m_{\mathrm{eff}}[(\omega_0^2-\omega^2)^2 + (\gamma_{\mathrm{m}}^2\omega^2)]}. \tag{3.16}$$

In thermal equilibrium, the mean mode energy of the harmonic mechanical oscillator, $\langle E\rangle$, is given by

$$\langle E\rangle = \frac{1}{2}m_{\mathrm{eff}}\langle \dot{x_{\mathrm{th}}}^2\rangle + \frac{1}{2}k\langle x_{\mathrm{th}}^2\rangle, \tag{3.17}$$

which should be equal to $\langle E\rangle = k_{\mathrm{B}}T$. From the equipartition theorem we get individual equilibration of the kinetic and the potential energies:

$$\frac{1}{2}m_{\mathrm{eff}}\langle \dot{x}_{\mathrm{th}}^2\rangle = \frac{1}{2}k\langle x_{\mathrm{th}}^2\rangle = \frac{1}{2}k_{\mathrm{B}}T. \tag{3.18}$$

Using the last equation and $k = m_{\mathrm{eff}}\omega^2$ we get

$$\langle x_{\mathrm{th}}^2\rangle = \frac{k_{\mathrm{B}}T}{m_{\mathrm{eff}}\omega_0^2}. \tag{3.19}$$

Furthermore, from equation (3.11) we obtain that the area under the single-sided mechanical thermal noise spectrum of a mechanical harmonic oscillator equals the variance of its displacement

$$\langle x_{\mathrm{th}}^2\rangle = \int_0^\infty \frac{1}{2\pi}d\omega S_x(\omega) = \frac{k_{\mathrm{B}}T}{m_{\mathrm{eff}}\omega_0^2}, \tag{3.20}$$

as illustrated in Figure 3.2.

[6] White noise is a random signal with constant *power spectral density*.

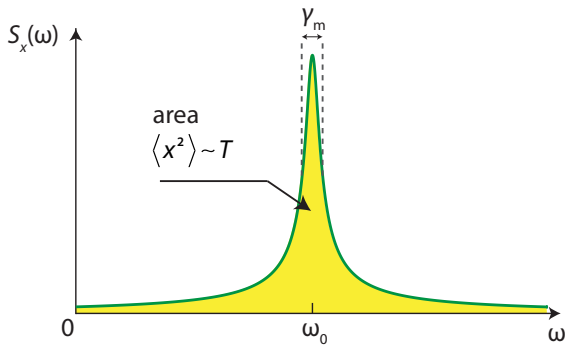

Figure 3.2: Noise spectrum of damped harmonic oscillator in thermal equilibrium.

3.2.2 Response to a coherent driving force

We now want to analyze the response of the damped harmonic oscillator to a coherent driving force. To do this, we solve the equation of motion (3.5) driven by a coherent force $F(t) = F_0 \cos(\omega_d t)$,

$$m_{\text{eff}} \frac{d^2x(t)}{dt^2} + kx(t) + m_{\text{eff}}\gamma_{\text{m}} \frac{dx(t)}{dt} = F_0 \cos(\omega_{\text{d}} t), \tag{3.21}$$

where F_0 is the driving amplitude and ω_{d} is the drive frequency. Working in the frequency domain, the amplitude $x(\omega_{\text{d}})$ is given by

$$x(\omega_{\text{d}}) = \frac{F_0/m_{\text{eff}}}{\sqrt{(\omega_0^2 - \omega_d^2)^2 + (\gamma_{\text{m}}\omega_d)^2}}, \tag{3.22}$$

and the phase $\phi(\omega)$ by

$$\phi(\omega_d) = \arctan\left(\frac{\gamma_m \omega_d}{(\omega_0^2 - \omega_d^2)}\right). \tag{3.23}$$

By applying an inverse Fourier transform, we can also obtain the displacement in time domain

$$x(t) = \frac{\omega_0}{\gamma_{\text{m}}} \frac{F_0}{m_{\text{eff}}\omega_0^2} \sin\omega_{\text{d}} t = Q \frac{F_0}{m_{\text{eff}}\omega_0^2} \sin\omega_d t. \tag{3.24}$$

On resonance ($\omega_d = \omega_0$), the motion is $\pi/2$ out of phase with the driving force (see Figure 3.3), and the motional amplitude is getting maximum, while it is proportional to the quality factor Q.

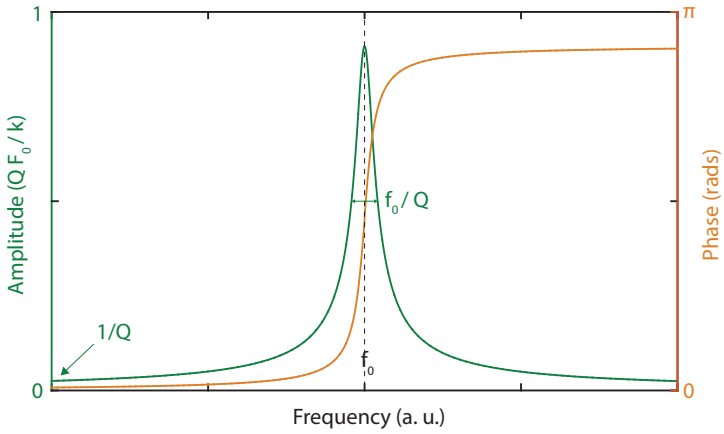

Figure 3.3: Amplitude and phase response of damped harmonic oscillator as a function of a sinusoidal driving force frequency. On resonance ($\omega_\mathrm{d} = \omega_0$), the motion amplitude is maximum and $\pi/2$ out of phase with the driving force.

3.3 Duffing oscillator

So far we have assumed that nanomechanical resonators can be described by the harmonic oscillator model, where the restoring force scales linearly with position, obeying Hooke's law. Usually this is a very good approximation since most of the materials that are used in nanomechanical systems, can sustain very high deformation before their linear strain-stress dependency breaks down. However, when driving mechanical resonators at large displacement amplitudes, very often nonlinearities appear in the restoring force of the harmonic oscillator model, much before the intrinsic limit of the materials that are made of. This behavior can be modeled by adding in the equation of motion a restoring force term that is proportional to the cube of the displacement. This is called the Duffing oscillator model and is written as

$$m_\mathrm{eff}\frac{d^2x(t)}{dt^2} + kx(t) + m_\mathrm{eff}\gamma_\mathrm{m}\frac{dx(t)}{dt} + \alpha x(t)^3 = F(t), \tag{3.25}$$

where α is the dimensionless nonlinear Duffing coefficient. Solving this equation in frequency space, we obtain the displacement amplitude

$$x(\omega_\mathrm{d}) = \frac{F_0/m_\mathrm{eff}}{\sqrt{(\omega_0^2 + \frac{3}{4}\alpha x(\omega_\mathrm{d})^2 - \omega_\mathrm{d}^2)^2 + \gamma_\mathrm{m}^2\omega_\mathrm{d}^2)}} \tag{3.26}$$

and the phase

$$\phi(\omega_\mathrm{d}) = \arctan\left(\frac{\omega_0\omega_\mathrm{d}}{\frac{\omega_0}{\gamma_\mathrm{m}}(\omega_0^2 + \frac{3}{4}\alpha x(\omega_\mathrm{d})^2 - \omega_\mathrm{d}^2)}\right). \tag{3.27}$$

Figure 3.4 illustrates the nonlinear amplitude and phase response of a duffing damped driven oscillator. At low drive force, the amplitude scales linearly with the drive force, as

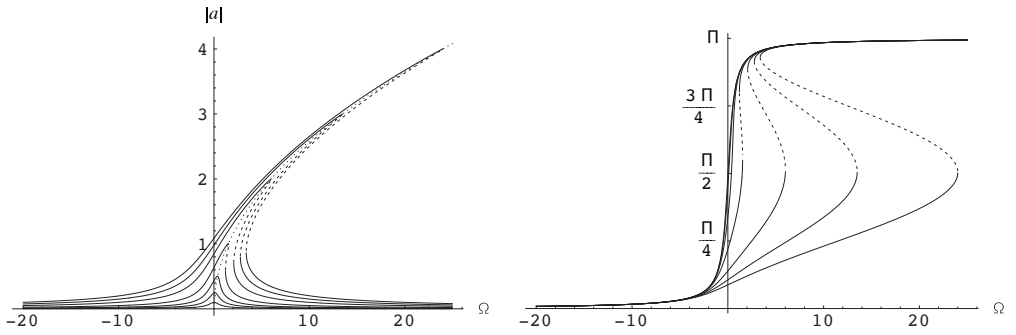

Figure 3.4: Amplitude and phase response of duffing oscillator to external sinusoidal driving force, for sequence of increasing values of the drive amplitude. Solid curves indicate stable solutions of the response function, while dashed curves indicate unstable solutions. Figure adapted from [67].

in a linear harmonic oscillator. As the driving force is increasing, the oscillator tends to get stiffer, and the resonance peak shifts towards higher or lower frequencies, depending on the sign of α. After a threshold on F_0, the displacement amplitude equation $x(\omega_d)$ has three solutions. The solution for intermediate amplitude is unstable, leaving the resonator bistable, oscillating between the two other solution. This phenomenon also appears as a hysteresis in its response, depending on the direction that the driving frequency is swept. The phase response also exhibits bistability and hysteresis.

The Duffing nonlinearity has various origins: It can be geometrical, especially in doubly-clamped beams, due to nonlinear external potentials, or due to nonlinearities in the transduction scheme. In general, duffing nonlinearity is a nuisance for practical application of nanomechanical resonators, mainly because it tends to decrease the dynamic range of these systems [66]. On the other hand, it can lead to systems with very rich dynamical behavior. For instance, coupled resonating systems [60] belong to this category and are part of extensive study in this Ph.D thesis, the results of which are discussed in chapter 5.

3.4 Nonlinear damping

Apart from the nonlinearity that appears in the restoring force of a mechanical resonator (conservative nonlinearity), nonlinearities often appear in the damping mechanisms that accompany every physical resonator (non-conservative nonlinearity), due to various physical mechanisms. This behavior is sufficiently modeled by adding, in the equation of motion, a term $\eta x(t)^2 \frac{dx(t)}{\mathrm{d}t}$. Eventually, the equation of motion that includes both duffing nonlinearity and nonlinear damping will be given by

$$m_{\mathrm{eff}} \frac{d^2x(t)}{dt^2} + kx(t) + m_{\mathrm{eff}} \gamma_{\mathrm{m}} \frac{dx(t)}{dt} + \alpha x(t)^3 + \eta x(t)^2 \frac{dx(t)}{\mathrm{d}t} = F(t), \tag{3.28}$$

where η is the coefficient of nonlinear damping. Solving this equation in the frequency space [67], we obtain the displacement amplitude

$$x(\omega_{\mathrm{d}}) = \frac{F_0/2m_{\mathrm{eff}}\omega_0^2}{\sqrt{(\frac{\omega_{\mathrm{d}}-\omega_0}{\omega_0} - \frac{3\alpha x(\omega_{\mathrm{d}})^2}{8m_{\mathrm{eff}}\omega_{\mathrm{d}}^2})^2 + (\frac{\gamma_{\mathrm{eff}}}{2\omega_0} + \frac{\eta x(\omega_{\mathrm{d}})^2}{8m_{\mathrm{eff}}\omega_0})^2}} \tag{3.29}$$

and the phase

$$\phi(\omega_{\mathrm{d}}) = \arctan\left(\frac{\frac{m_{\mathrm{eff}}\gamma_{\mathrm{eff}}}{2} + \frac{\eta x(\omega_{\mathrm{d}})^2}{8}}{m_{\mathrm{eff}}(\omega_{\mathrm{d}}-\omega_0) - \frac{3\alpha x(\omega_{\mathrm{d}})^2}{8\omega_0})}\right). \tag{3.30}$$

Chapter 4

Transduction techniques

In this chapter we will give an overview of the main transduction techniques that are commonly employed in graphene and carbon nanotube mechanical resonators. Some of them have been used and further developed during this thesis.

We will first start with the electrical transduction schemes[1]. We will discuss the actuation, the read out, and we will emphasize on the widely used, also in chapter 5 of this thesis, electrical frequency mixing techniques. We will additionally present the direct transduction schemes as well as a superconducting cavity-based scheme that we developed for graphene resonators and is reported in Ref. [68]. We will then discuss the optical transduction schemes as implemented for graphene or carbon nanotube resonators, and finally we also discuss various microscopy techniques. More details on specific transduction schemes will also be included in specific chapters of this thesis.

4.1 Introduction

The motion transduction of nanomechnical resonators is one of the field's central challenges. The exploitation of the potential of these devices inevitable requires accurate read-out and external control of their motion. Therefore, several actuation and detection schemes have been developed and utilized in various vibrating nanomechanical systems. For instance, optical [69], magnetomotive [70, 71], piezoelectric [72], piezoresistive [73], and electrostatic [18, 74, 75] techniques. Nonetheless, due to the intrinsic low dimensionality of resonators which are based on graphene and carbon nanotubes, the efficient actuation and detections of their motion is even more challenging and not all the above techniques are suitable. In this chapter, an overview of the state of the art of the transduction techniques for graphene and carbon nanotube resonators will be presented and analyzed.

4.2 Overview of electrical transduction techniques

[1] We will emphasize on the electrical transduction schemes as there are the most widely utilized for carbon nanotube and graphene resonators, and were extensively employed in chapter 5.

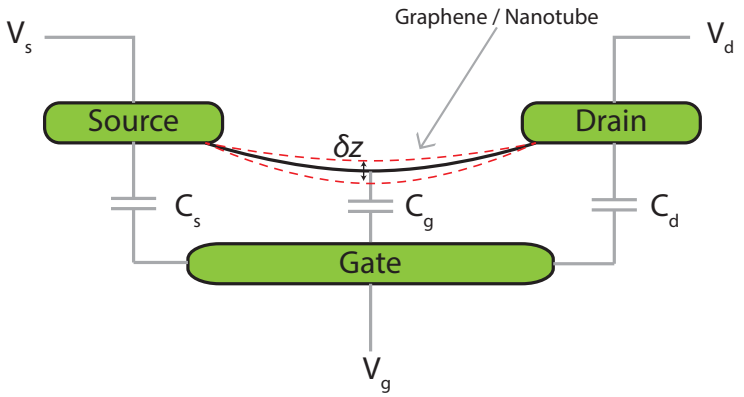

Figure 4.1: Schematic of a 3-terminal-configuration graphene/nanotube resonator. To optimize the electrical transduction efficiency of graphene's or nanotube's motion, the parasitic capacitances $C_{\rm s}$ and $C_{\rm d}$ should remain minimum with respect to the graphene/nanotube capacitance $C_{\rm g}$ to the gate.

4.2.1 Electrical actuation

A typical configuration of a graphene/nanotube mechanicalresonator, where electrical transduction techniques can be utilized, is illustrated in Figure 4.1. It is a three-terminal configuration, similarly to a transistor, where graphene/nanotube acts like the conducting channel, while it is suspended and free to mechanically vibrate. The graphene/nanotube is contacted by the source and drain electrodes while suspended above a gate, which could either be a local electrode or just the highly doped silicon substrate which is acting as a global back gate. By applying a DC bias to the back gate, the graphene/nanotube is statically deflected towards it. The device is actuated, at this equilibrium position, by applying an additional oscillating potential at frequency ω to the back gate. This will lead to an oscillating force

$$F = -\frac{1}{2}\frac{\partial C_{\rm g}}{\partial z}(V_{\rm g} + \delta V_{\rm g})^2 \Rightarrow \delta F \approx C_{\rm g}^{'} V_{\rm g} \delta V_{\rm g}, \tag{4.1}$$

where z is the distance and $C_{\rm g}$ the capacitance between the graphene/nanotube and the gate electrode. At resonance, graphene/nanotube vibrates around its static position and the system acts as a simple harmonic oscillator with restoring force $F = -k\delta x$ and resonant frequency $f_0 = \frac{1}{2}\sqrt{\frac{k}{m_{\rm eff}}}$, where $m_{\rm eff}$ is the effective mass. This driving scheme can be used in conjunction not only with electrical but with optical read-out as well.

4.2.2 Electrical readout

The electrical readout is based on the field-effect and capacitive characteristics of these devices. The conductance of graphene and semiconducting nanotubes depends on their charge, which depends on the position z, due to the change of the capacitance $C_{\rm g}$, and on the gate voltage $V_{\rm g}$, due to the field-effect. Expanding around $V_{\rm g}$ and x, small changes of conductance in time can be expressed as

$$G(V_{\rm g}, x) = G(V_{\rm g}) + \frac{dG}{dV_{\rm g}}\ \delta V_{\rm g} + \frac{dG}{dz}\ \delta z \Rightarrow \delta G(t) = \frac{dG}{dV_{\rm g}}\ \delta V_{\rm g}(t) + \frac{dG}{dz}\ \delta z(t). \tag{4.2}$$

The first term is purely electrical, standard transition gating effect, while the second term is mechanical and appears only if the graphene/nanotube is moving. This allows the transduction of their motion into a time varying current at their drain:

$$\delta I(t) = V_{\rm sd}\delta G(t). \tag{4.3}$$

The dependence of the conductance on the deflection of the graphene/nanotube can be expressed as

$$\frac{dG}{dz} = \frac{dG}{dQ}\frac{dQ}{dz}. \tag{4.4}$$

The dependence of the conductance to the charge is given by

$$\frac{dG}{dQ} = \frac{dG}{dV_{\rm g}}\frac{dV_{\rm g}}{dQ} = \frac{dG}{dV_{\rm g}}\frac{1}{C_{\rm g}}, \tag{4.5}$$

and the dependence of the charge to the deflection is given by

$$\frac{dQ}{dz} = \frac{\partial Q}{\partial z}\frac{dz}{dz} + \frac{\partial Q}{\partial V_{\rm g}}\frac{dV_{\rm g}}{dz} = \frac{\partial (C_{\rm g}V_{\rm g})}{\partial z} = V_{\rm g}\frac{\partial C_{\rm g}}{\partial z} = V_{\rm g}\frac{\partial C_{\rm g}}{\partial z}$$

$$\Rightarrow \frac{dQ}{dz} = V_{\rm g}C'_{\rm g}. \tag{4.6}$$

Using equations (4.5) and (4.6) the conductance on the deflection is given by

$$\frac{dG}{dz} = V_{\rm g}\frac{C'_{\rm g}}{C_{\rm g}}\frac{dG}{dV_{\rm g}}. \tag{4.7}$$

Equation (4.3) can be then expressed as

$$\delta G(t) = \frac{dG}{dV_{\rm g}}\ \delta V_{\rm g}(t) + V_{\rm g}\frac{C'_{\rm g}}{C_{\rm g}}\frac{dG}{dV_{\rm g}}\ \delta z(t) \tag{4.8}$$

As a result, the total time-depended current measured at the drain is given by

$$I_{\rm d}(t) = V_{\rm sd}\ [G(V_{\rm g}) + \delta G(t)] \tag{4.9}$$

$$\Rightarrow I_{\rm d}(t) = V_{\rm sd}\ G(V_{\rm g}) + V_{\rm sd}\ \frac{dG}{dV_{\rm g}}\delta V_{\rm g}(t) + V_{\rm g}\frac{C'_{\rm g}}{C_{\rm g}}\frac{dG}{dV_{\rm g}}\delta z(t). \tag{4.10}$$

The first term corresponds to the DC current, which depends on the source and the DC gate biasing, while the second term is a time-varying component purely electrical due to the small time-varying changes at the back gate biasing. The last term is electromechanical and depends on the time-varying deflection of the graphene/nanotube. For high electron mobility graphene or nanotube tube devices, where the transconductance ($dG/dV_{\rm g}$) is very large, the electromechanical current can be significant compared to other nanoresonators with similar dimensions made out of materials with much lower transconductance. In reality though, the ability to read it out is restricted by the relative low bandwidth of the transistor based layout of these devices (see more details in the next section), mainly due to the very high parasitic capacitances, and the difficulty to match their electrical impedance characteristics. Additionally, Johnson-Nyquist noise further reduces the read out sensitivity depending on the experimental temperature.

4.2.3 Readout bandwidth

Taking as an example a graphene resonator, assuming that graphene acts as a ballistic conductor, it can be simply modeled with one contact resistor and one parasitic capacitor to the gate, for each of the source and drain electrodes (Figure 4.1). The resistor and the capacitor at the drain of the device forms a low pass filter, with a cut-off frequency which defines the available readout bandwidth in which we can detect the electromechanical signal. The cut-off frequency is given by the expression

$$f_{\text{cutoff}} = \frac{1}{2\pi R_{\text{d}} C_{\text{d}}}. \tag{4.11}$$

Assuming a device with 2-point resistance in the order of 20 KΩ and assuming that this is shared symmetrically between the source and the drain, this gives $R_{\text{d}} = 10$ KΩ. For a device with a global back gate, the parasitic capacitance of each electrode can be simple calculated with a parallel plate capacitor model

$$C = \frac{\epsilon_0 \epsilon A}{d}, \tag{4.12}$$

where ϵ_0 is the dielectric permitivity of vacuum, ϵ the relative permitivity, A the area of the capacitor, and d the distance between the two plates of the capacitor. For electrodes of 250 μm x 250 μm and SiO_2 dielectric of 435 nm thickness, the parasitic capacitor for the drain electrode is $C_{\text{d}} = 62.5$ nF. Using equation (4.11) the cut-off frequency for this specific graphene device is estimated to be at 3.2 MHz. The typical graphene resonators that were investigated during this thesis had resonance frequencies ranging from few tens to few hundreds of MHz, and hence very difficult to detect their motion. Most of the high frequency signal would be lost into the parasitic capacitances. For carbon nanotube devices where the contact resistance is on average higher compared to graphene, the cutoff limit can be even lower. Furthermore, the extra parasitic capacitances due to the wiring of the measurement system, can even further decrease the estimated cut-off limit.

4.2.4 Frequency mixing techniques

The limited available bandwidth is very common obstacle in nano-scale electron devices, therefore various techniques have been developed to overcome it. One approaches is to parametrically down-convert the high frequency signal below the cut-off frequency of the device. This method has been used in a nanomechanical resonator coupled to a single electron transistor [76] and later on in doubly-clamped carbon nanotube and graphene resonators [18, 19].

The basic idea is to make use of the non-zero transconductance dG/dV_g of graphene or nanotube devices, and utilize them as frequency mixers of different oscillating potentials that are applied at the ports of the device. This way it is possible to encode the vibration information of the device at new frequency, which can be below the cut-off limit of the device. Different versions and variants of the frequency mixing techniques exist, all of them sharing the same philosophy. The most broadly used versions and systemically employed during this thesis are the two-source mixing, the amplitude modulation (AM) mixing, and the frequency modulation (FM) mixing.

Two-source mixing technique

Sazonova *et al.* [18] was the first to demonstrate an electrical motion transduction of a double clamped semiconducting carbon nanotube using the two source mixing technique, while Chen *et al.* [19] used the same method to firstly demonstrate the motion transduction of a double clamped graphene resonator. The layout of this transduction scheme is depicted in Figure 4.2.

To realize the two-source frequency mixing technique, a $V_{\rm g} + \delta V_{\rm g}\ \cos\omega t$ potential is applied at the gate, and one that is detuned by $\Delta\omega$, $\delta V_{\rm sd}\cos((\omega+\Delta\omega)t)$, at the source. Similarly as in equation 4.9, the time dependent current at the output can be expressed as

$$I_{\rm d}(t) = V_{\rm sd}^{\omega+\Delta\omega}\,[G(V_{\rm g}) + G^{\omega}] \tag{4.13}$$

$$= V_{\rm sd}^{\omega+\Delta\omega}\,G(V_{\rm g}) + V_{\rm sd}^{\omega+\Delta\omega}\,G^{\omega} \tag{4.14}$$

The first term of the last expression describes the current at the frequency of the $V_{\rm sd}^{\omega+\Delta\omega}$ potential, while the second term is responsible for the mixing process since components of ω and $\omega+\Delta\omega$ are mixed together:

$$V_{\rm sd}^{\omega+\Delta\omega}\,G^{\omega} = \delta G\ \cos\omega t\cdot\delta V_{\rm sd}\ \cos((\omega+\Delta\omega)t) \tag{4.15}$$

$$= \frac{1}{2}\,\delta G\,\delta V_{\rm sd}\cdot[\cos(2\omega t) + \cos(\Delta\omega t)]. \tag{4.16}$$

After the mixing process, the current at the drain of the device has two more frequency components, one at 2ω and one at $\Delta\omega$. The mixing current at $\Delta\omega$ is given by

$$I_{\rm d}^{\Delta\omega}(t) = \frac{1}{2}\,\delta G\,\delta V_{\rm sd}\ \cos(\Delta\omega t) \tag{4.17}$$

$$= \frac{1}{2}\delta V_{\rm sd}\cdot[\frac{dG}{dV_{\rm g}}\delta V_g + V_g\frac{C_g'}{C_g}\frac{dG}{dV_{\rm g}}\delta z(t)]\ \cos(\Delta\omega t) \tag{4.18}$$

$$\Rightarrow I_{\rm d}^{\Delta\omega}(t) = \frac{1}{2}\delta V_{\rm sd}\frac{dG}{dV_{\rm g}}\cdot[\delta V_{\rm g} + V_{\rm g}\frac{C_{\rm g}'}{C_{\rm g}}\delta z(t)]\ \cos(\Delta\omega t) \tag{4.19}$$

The first term of this expression is purely electrical and contains no information on the mechanics. The second term though, directly depends on the amplitude of the graphene/nanotube motion $\delta z(t)$, enabling the detection of the high frequency mechanically oscillation by monitoring the current at the mixing frequency $\Delta\omega$. This frequency can be selected as small as it needed in order to be below the cutoff of frequency of the device. By using lock-in techniques it is possible to detect $I_{\rm d}^{\Delta\omega}$ with very high sensitivity, avoiding the direct pickup of the RF capacitive background.

Amplitude modulation mixing technique (AM)

Another way to achieve similar results to the two source mixing is to apply an amplitude modulated (AM) oscillating potential at the source of the device, and a static potential at the gate (Figure 4.3). The AM modulation of an arbitrary signal $\delta V\ \cos\omega t$ is defined as

$$V^{\rm AM}(t) = [1 + m\ \cos(\Delta\omega t)]\cdot A\ \cos(\omega t) \tag{4.20}$$

$$= \delta V\ \cos(\omega t) + \frac{\delta V\ m}{2}[\cos((\omega+\Delta\omega)t) + \cos((\omega-\Delta\omega)t)], \tag{4.21}$$

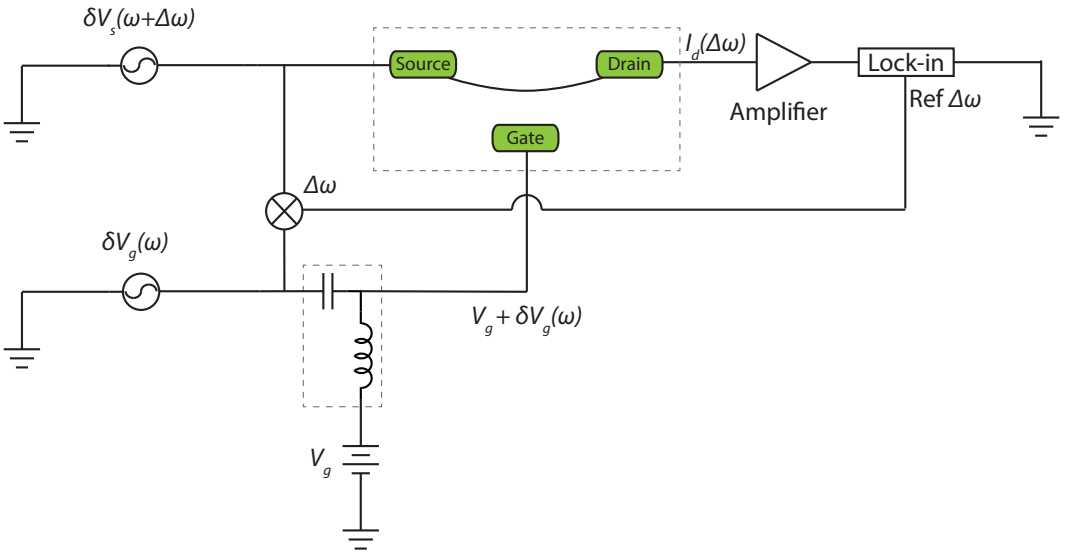

Figure 4.2: Two-source mixing transduction scheme.

where ω is the carrier frequency, m the modulation strength, and $\Delta\omega$ the modulation frequency. The AM signal consists of three frequency components, one at ω and two sideband frequencies at $\omega \pm \Delta\omega$, which are enough to provide both the driving and the conductance modulation needed for the readout. In this case the graphene/nanotube doesn't act as a mixer but as a demodulator of the already modulated signal. This technique, in terms of the resulting mixing current, is equivalent to a two source mixing where

$$\delta V_{\mathrm{g}} = V_{\mathrm{sd}}\ \cos(\omega t) \tag{4.22}$$

$$\delta V_{\mathrm{sd}} = \delta V_{\mathrm{sd}}^{\mathrm{AM}}\ m\ \cos((\omega + \Delta\omega)t). \tag{4.23}$$

Consequently the drain current at $\Delta\omega$ is given by

$$I_{\mathrm{d}}^{\mathrm{AM}\ \Delta\omega}(t) = \frac{m}{2}\delta V_{\mathrm{sd}}\frac{dG}{dV_{\mathrm{g}}} \cdot [\delta V_{\mathrm{g}} + V_{\mathrm{g}}\frac{C_{\mathrm{g}}'}{C_{\mathrm{g}}}\delta z(t)]\ \cos(\Delta\omega t). \tag{4.24}$$

Frequency Modulation mixing technique (FM)

Frequency modulation (FM) mixing has been employed both in carbon nanotubes and on graphene resonators [77, 78, 13]. As the AM technique, it is a single-source, where a frequency modulated oscillating potential is applied at the source and a static potential at the gate (Figure 4.3). A frequency modulated signal is defined as

$$V^{\mathrm{FM}}(t) = \delta V\cos(\omega t + (\omega_\Delta/\omega_{\mathrm{L}})sin(\omega_{\mathrm{L}}t)), \tag{4.25}$$

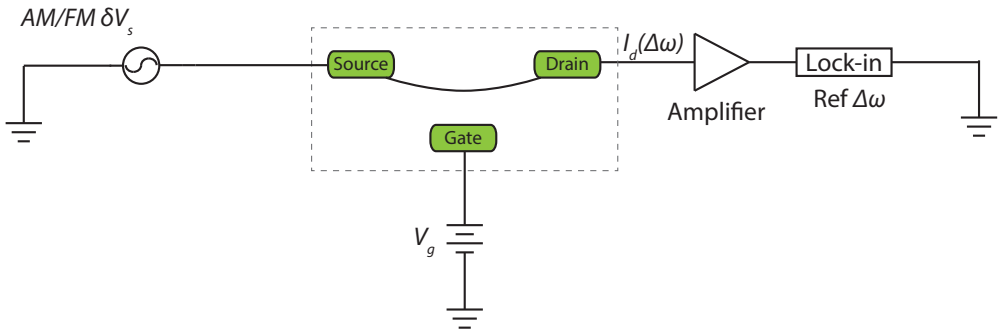

Figure 4.3: AM/FM mixing transduction scheme.

where ω is the carrier frequency, ω_Δ the frequency deviation, and ω_L the modulation frequency. The resulting low frequency mixing current at the drain is given by

$$I_\mathrm{d}^{\mathrm{FM}\,\Delta\omega}(t) = \frac{1}{2}\frac{dG}{dV_\mathrm{g}} V_\mathrm{g}\,\delta V_\mathrm{g}\,\frac{C'}{C}\,\omega_\Delta\,\frac{\partial}{\partial\omega} Re[\delta z(t)] \tag{4.26}$$

where $Re[x_0]$ the real part of its vibration amplitude.

An advantage of the FM mixing technique, in comparison to the AM and to the two-source, is that more efficiently rejects the undesirable electrical background noise and keeps only the signals that originates from the mechanical motion. Indeed, according to equation 4.26 the measured signal lacks any pure electrical term and contains only electromechanical terms. The down-mixed current is proportional to the derivative of the real part of the complex Lorentzian response function of the resonator. As a result, the measured lineshape is not Lorentzian and the absolute value of it shows two minima (Figure 4.4(b)). For a weakly damped linear resonator, the separation of these minima, Δf, coincides with the mechanical bandwidth defined as FWHM for the squared modulus of the motional amplitude (time-averaged mechanical energy stored) and allows to extract the quality factor Q in a simple manner from the relation $\Delta f = f_0/\Delta f$ [77, 13].

Other electrical mixing transduction techniques

Another variation of the mixing transduction techniques has been used by Moser *et al.* [23, 17] to measure the thermal vibration and perform force sensitivity experiments on ultra high quality factor nanotube resonators at cryogenic temperature. The schematic of the setup is illustrated in Figure 4.5. A weak oscillating potential $V_\mathrm{sd}(\omega_\mathrm{mod})$ is applied on the source electrode, few tens of kilohertz away from the resonance frequency, in order to parametrically down-convert the signal that is measured at the output/drain of the device and avoid bandwidth issues, in a similar manner as the previously described down-mixing techniques. The resulting current fluctuations on the drain electrode are described by

$$\delta I^{|\omega-\omega_\mathrm{mod}|}(t) = V_\mathrm{sd}^{\omega_\mathrm{mod}}\delta G = V_\mathrm{sd}^{\omega_\mathrm{mod}}\frac{dG}{dV_\mathrm{g}} V_\mathrm{g}\,\frac{C'_\mathrm{g}}{C_\mathrm{g}}\,\delta z(t)\,\cos(\omega_\mathrm{mod}t). \tag{4.27}$$

The current fluctuations $\delta I(t)$ at the output are converted to voltage fluctuations $\delta V_R(t)$ across a resistor R. The novelty of this technique is that this signal is split and amplified

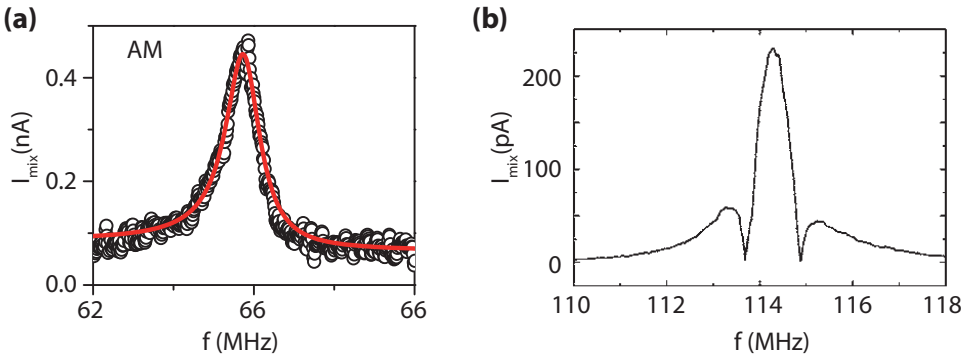

Figure 4.4: AM-FM mixing techniques measurement examples. **(a)** Mechanical resonance measured using the AM mixing technique. Figure adapted from [28]. **(b)** Mechanical resonance measured using the FM mixing technique. Figure adapted from [77].

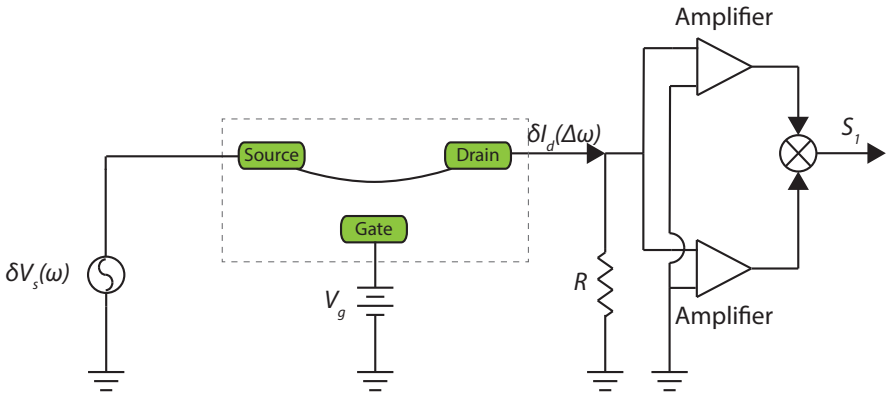

Figure 4.5: Cross-correlation measurement scheme.

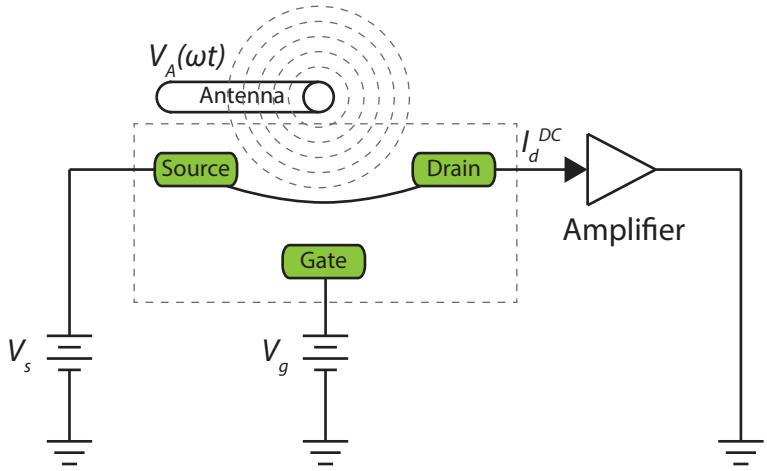

Figure 4.6: Rectification transduction scheme.

by two independent low-noise amplifiers and then cross-correlated using an Fast Fourier spectrum analyzer. This method cancels out the voltage noise of the amplifiers and considerably increases the signal-to-noise ratio of the setup.

A transduction scheme that resembles mixing techniques has been used by Hüttel *et al.* (2009) [16] to detect the vibrations of carbon nanotubes at low temperatures. Essentially, this technique parametrically down-converts signal from MHz range to DC, therefore the carbon nanotube resonator acts as rectifier. The layout of this scheme is illustrated in Figure 4.6. A micro-antenna close to the device electrostatically actuates it, while DC bias is applied at the source and at the gate. The crucial point of this technique is that the nanotube is in the coulomb blockade regime and its transconductance is highly nonlinear in the vicinity of the coulomb oscillations. Hence, on the contrary to the aforementioned mixing techniques, higher order terms in the Taylor expansion of the conductance cannot be neglected. It can be shown that by including the second order terms there is a DC component at the drain current which directly depends on the motion of the nanotube and is given by

$$I_{\mathrm{d}}^{\mathrm{DC}}(t) = \frac{1}{4} V_{\mathrm{sd}} \frac{d^2 G}{dV_{\mathrm{g}}^2} \left(\frac{V_{\mathrm{g}} C_{\mathrm{g}}'}{C_{\mathrm{g}}} \right)^2 d^2 x(t). \tag{4.28}$$

Similarly to the mixing techniques, the mechanical vibration can be detected, bypassing the bandwidth limitations of the devices, by measuring the DC current at the drain. Another advantage is that there is no need for high frequency cabling connected directly to the device and this way heating at low temperature is minimized. The shortcomings are related to the necessity of devices with very nonlinear transconductance, as a nanotube in the coulomb blockade regime, and to the existence of higher $1/f$ noise at DC.

Another version of the mixing techniques has been developed by Schneider *et al.* (2014) [79] to perform ring-down measurements for the first time. The nonlinearities of nanotube's transconductance at low temperatures allow to mix an actuation oscillating potential and a local oscillator, which are applied at the bagk-gate and are 7 MHz detuned, resulting in a downmixed electromechanical signal at the detuning frequency. This rela-

tively high mixing frequency in addition to a High Electron Mobility Transistor (HEMT) amplifier at the drain, provides enough bandwidth to perform ring-down experiments.

4.2.5 Direct electrical transduction

Mixing techniques have been used with great success in investigating the fundamental properties [18, 24, 25, 13] and exploring the sensitivity limits [20, 23] of these nano-scale objects. Nonetheless, the process of down mixing results in a great reduction of the available bandwidth which is a drawback for applications requiring real time detection, like high speed sensing or signal processing. Xu *et al.* [80] have shown that it is possible to directly read out the motion of a graphene resonator without any parametric down-conversion processing. To achieve this, they employed devices with local gate structure on a highly resistive substrate in order to minimize their parasitic capacitances. This allowed for a direct readout using a vector Network analyzer (VNA) in a circuit layout which is shown in (Figure 4.7). The RF current through the device is given by

$$I_{\mathrm{d}}^{\mathrm{RF}}(t) = j2\pi f C_{\mathrm{g}}\left(\frac{C_{tot}}{C_{\mathrm{g}}}\delta V_{\mathrm{g}} - V_{\mathrm{g}}\frac{C'_{\mathrm{g}}}{C_{\mathrm{g}}}\delta z(t)\right) + V_{\mathrm{d}}\frac{dG}{dV_{\mathrm{g}}}\left(\delta V_{\mathrm{g}} - V_{\mathrm{g}}\frac{C'_{\mathrm{g}}}{C_{\mathrm{g}}}\delta z(t)\right), \tag{4.29}$$

where C_{g} is the capacitance between the graphene and the local back gate, and C_{tot} the total capacitance of the device including the parasitic capacitances. The first parenthesis of equation 4.29 contains the capacitive terms, where the first term is pure electrical while the second is electromechanical. The second parenthesis contains terms that arise from the transconductance properties of graphene, where the first is purely electrical and the second electromechanical. On the contrary to Si-based MEMS where the main signal comes from the capacitive terms, due the their large area, in graphene the majority of the signal arises due to the high transconductance of graphene.

4.2.6 Cavity-based electrical transduction schemes

Apart from the direct transduction scheme, which we described in the previous section, another way to avoid parametrical down-conversion of the electromechanical signal is to capacitively couple the motion of a mechanical resonator to the energy that is stored in a microwave or an RF cavity resonator. Such systems have been used in the field of optomechanics [81] in order to study mechanical motion in the quantum regime [8], offering very high readout sensitivity and bandwidth.

In our work [68], we demonstrated an integrated system where a graphene mechanical resonator is capacitively coupled to a superconducting microwave cavity (Figure 4.8). A superconducting cavity can be modeled as *RLC*-circuit where the resonant angular frequency is given by

$$\omega_{\mathrm{c}} = \frac{1}{\sqrt{LC_{\mathrm{tot}}}}, \tag{4.30}$$

where L is the total inductance and C_{tot} is the total capacitance of the superconducting cavity. In the design process, these values are usually selected to give resonant frequency of few GHz, which provides enough bandwidth to readout graphene's motion in real-time, while the photon occupation is low at mK temperatures ($\hbar\omega_{\mathrm{c}} < k_{\mathrm{B}}T$), which is critical for optomechanical experiments [81]. For the device that is depicted in Figure 4.8, $C_{\mathrm{tot}} \approx 90$ fF and $L \approx 6.3$ nH result in a cavity resonant frequency of $\omega_c/2\pi \approx 6.7$ GHz.

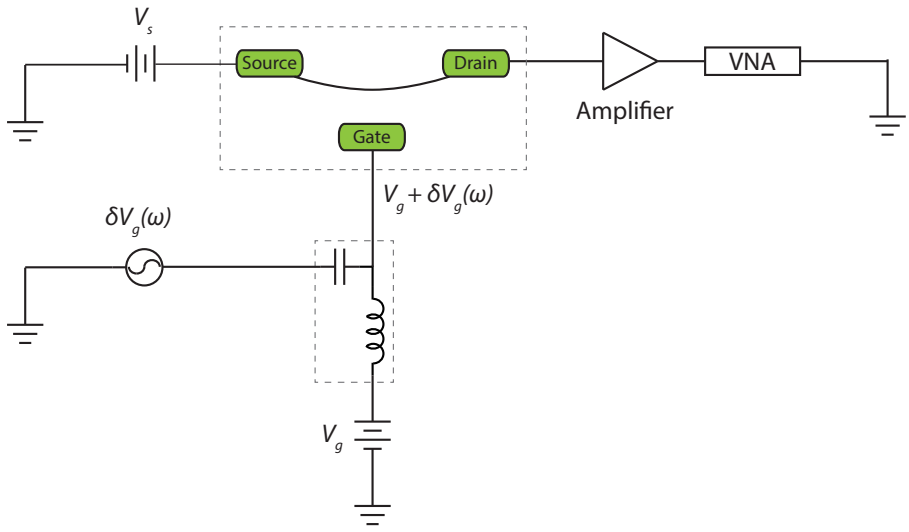

Figure 4.7: Direct RF transduction scheme.

The total capacitance $C_{\rm tot} = C + C_{\rm ext} + C_{\rm m}(z)$ effectively consists of a cavity capacitance C, a contribution $C_{\rm ext}$ from the external feedline, and importantly, a contribution $C_{\rm m}(z)$ that depends on the graphene position z, which arises from the graphene acting as a moving capacitor plate. A small displacement z therefore produces a shift in $\omega_{\rm c}$ quantified by the coupling $G_0 = \frac{\partial \omega_{\rm c}}{\partial z}$. As a result, the interaction between the mechanical resonator and the superconducting cavity can be described by the Hamiltonian $H_{\rm int} = \hbar G_0 n_{\rm p} z$ [8] with $n_{\rm p}$ the number of pump photons in the cavity. The characteristic coupling at the level of the zero-point motion $z_{\rm zp} = \sqrt{\hbar/2m_{\rm eff}\omega_{\rm m}}$ is given by the so-called single-photon coupling $g_0 = G_0 z_{\rm zp}$, with $m_{\rm eff}$ the effective mass and $\omega_{\rm m}/2\pi$ the resonance frequency of the mechanical mode of interest.

In order to detect the vibrations of the graphene resonator, the open-end of the superconducting cavity is coupled to a microwave transmission line through the capacitance $C_{\rm ext}$. The transmission line is used to pump the superconducting cavity at frequency $\omega_{\rm p}/2\pi$ with input power $P_{\rm p,in}$. The transmission line is also employed to measure the output power $P_{\rm out}$ of the cavity at the frequency $\omega_{\rm c}/2\pi$. $P_{\rm out}$ is amplified at 4 K by a high-electron-mobility transistor (HEMT) with a noise temperature of about 2 K and measured in a spectrum analyzer (see schematic in Figure 4.8(d)).

The principle of the vibration readout is analogous to Stokes and anti-Stokes Raman scattering. By pumping the cavity at $\omega_{\rm p}$, sidebands in energy are created at $\omega_{\rm p} \pm \omega_{\rm m}$ due to the coupling of the photons with the mechanical motion. If the pump is detuned such that the upper sideband frequency is matched with the cavity resonance frequency $\omega_{\rm c} = \omega_{\rm p} + \omega_{\rm m}$ (see Figure 4.8(e)), the anti-Stokes scattering is resonantly enhanced. If $\omega_{\rm m}$ is significantly larger than the linewidth κ of the cavity, the rate of the anti-Stokes scattering per phonon is given by $\Gamma_+ \approx 4 n_{\rm p} g_0^2/\kappa$, with $n_{\rm p} \propto P_{\rm p,in}(\omega_{\rm p})$ the number of photons in the cavity. The mechanical vibrations can be detected by recording the output

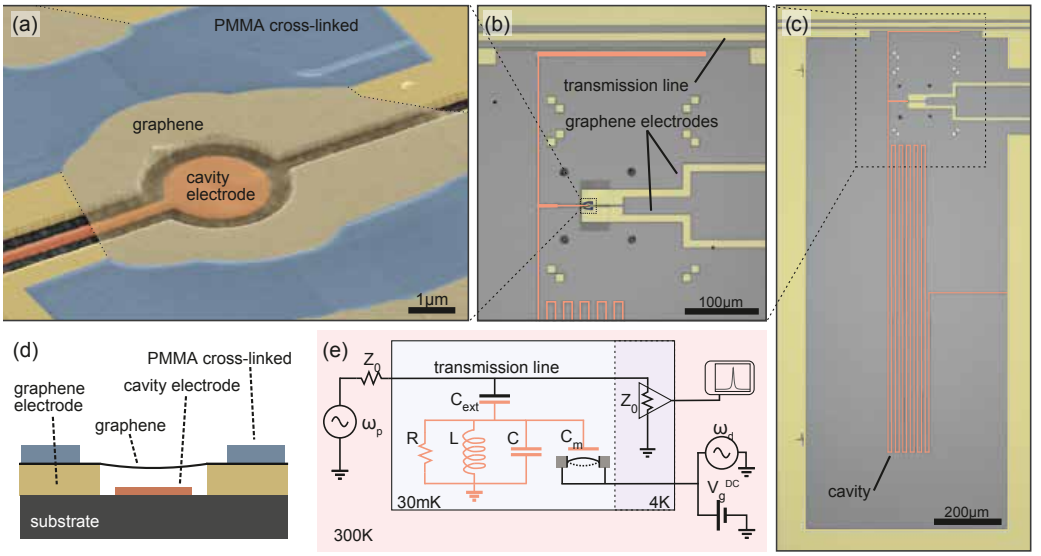

Figure 4.8: Graphene drum resonator coupled to a superconducting cavity. **(a)** False color SEM image of a circular graphene resonator capacitively coupled to a cavity electrode (red). The graphene sheet is clamped inbetween cross-linked PMMA (blue) and graphene support electrodes (yellow). **(b,c)** Optical microscope images of the superconducting cavity (red), two electrodes contacting the graphene flake (yellow, situated on the right-side of b and c), and a capacitively coupled transmission line (yellow, situated at the top in b and c). **(d)** Measurement schematic for the detection of the mechanical motion. Coherent pump ω_p and drive ω_d fields are applied to the transmission line and the graphene mechanical resonator, respectively. A constant voltage V_g^DC is applied to the graphene. The microwave signal from the cavity is amplified at 4 K with a HEMT amplifier and recorded at room temperature with a spectrum analyzer. **(e)** If the pump frequency is detuned such that $\omega_\mathrm{p} = \omega_\mathrm{c} - \omega_\mathrm{d}$, anti-Stokes scattering with phonons at rate Γ_+ leads to a detectable photon population at ω_c.

power at ω_c, which is given by

$$P_\mathrm{out} = P_\mathrm{p,in} \frac{\kappa_{ext}^2}{\kappa^2 + 4(\omega_\mathrm{c} - \omega_\mathrm{p})^2} 4 \frac{g_0^2}{\kappa^2} \frac{\langle z(t)^2 \rangle}{2 z_\mathrm{zp}^2}. \tag{4.31}$$

The graphene resonator can be actuated by applying a constant voltage V_g^DC and an oscillating voltage with amplitude V_g^AC at a frequency $\omega_\mathrm{d}/2\pi$ close to $\omega_\mathrm{m}/2\pi$ so that $\omega_\mathrm{d} = \omega_\mathrm{c} - \omega_\mathrm{p}$. As a result, the graphene resonator vibrates at $z(t) = \hat{z} \cos(\omega_\mathrm{d} t + \phi)$ with ϕ the phase difference between the displacement and the driving force.

Figures 4.9(b,c) show the resonance of the driven vibrations for the fundamental modes of two different devices, A and B. Modes at higher frequencies are observed as well, but they are hardly detectable. For device A the mechanical quality factor is $Q_m = \omega_m/\gamma_m \approx 100,000$ from the linewidth of the resonance $\gamma_m/2\pi = 575$ Hz. The photon number for this measurement is $n_\mathrm{p} = 8000$, so that $\Gamma_\mathrm{opt}/2\pi \approx 0.12$ Hz. With these parameters, the measurement imprecision, estimated to be 2.5 pm/$\sqrt{\mathrm{Hz}}$, and is limited by the noise of the low-temperature HEMT amplifier.

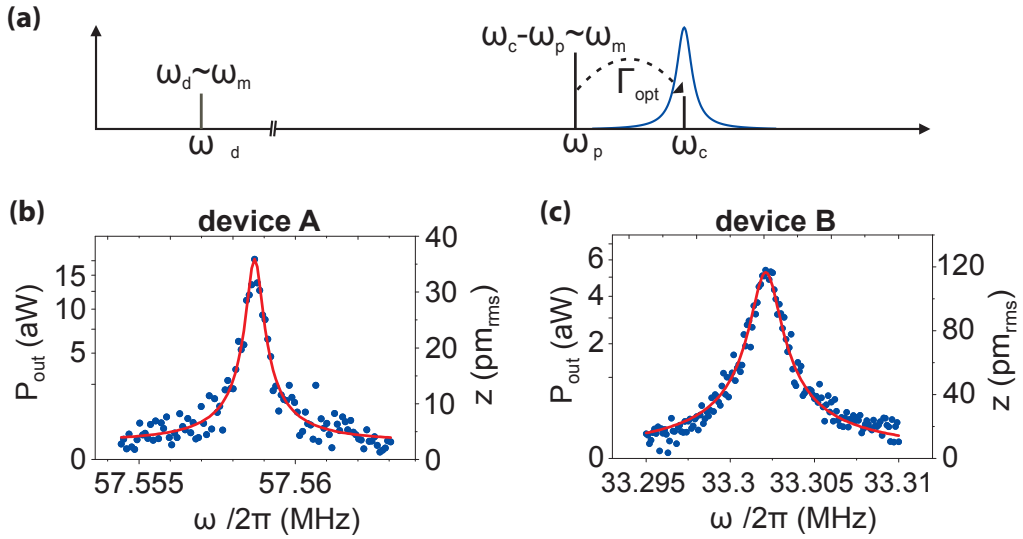

Figure 4.9: Detecting graphene's motion using a superconducting cavity. **(a)** Measurement scheme: If the pump frequency is detuned such that $\omega_p = \omega_c - \omega_m$, anti-Stokes scattering with phonons at rate Γ_{opt} leads to a detectable photon population at ω_c. **(b),(c)** Sideband measurement of the mechanical motion for device A with $V_g^{DC} = -2.894$ V and $V_g^{AC} = 190$ nV, and for device B with $V_g^{DC} = 3.405$ V and $V_g^{AC} = 4.3$ μV. Red lines are Lorentzian fits to the data which yield a mechanical quality factor of $Q_m = 100,000$ in device A and $Q_m = 17,700$ in device B. The calculated motional rms amplitude z is plotted on the right scale.

Similar transduction schemes for graphene resonators have been demonstrated by [30, 82, 83].

4.3 Overview of optical transduction techniques

The motion transduction of carbon nanotube resonators using a optical means represents a great challenge due their sub-wavelength dimensions which results into a poor overlap with an optical beam [84]. Nonetheless, Sawano *et al.* [85] showed that is possible to measure the vibration of nanotube cantilevers in water using an optical detection transduction scheme. Later, Stapfner *et al.* [86] succeeded to resolve the thermal motion of a doubly-clamped nanotube resonator optically at room temperature, by placing it inside a fiber-based, high-finesse optical microcavity (Figure 4.10 **(a)**). The cavity is pumped using a stabilized diode laser at 780 nm while the nanotube is placed at the slope of the cavity resonance. The nanotube vibrations are analyzed by probing the reflected optical noise with a photo-diode where a spectrum analyzer is plugged at its output(Figure 4.10 **(b)**).

On the contrary, the transduction of graphene's motion with optical means is a very common approach [22, 87, 88, 78, 89, 90]. The majority of the transduction schemes are very similar to the experimental setup used by Bunch *et al.* [22] (see Figure 4.11), which is the first study where vibrations of suspended graphene were detected. In an optical

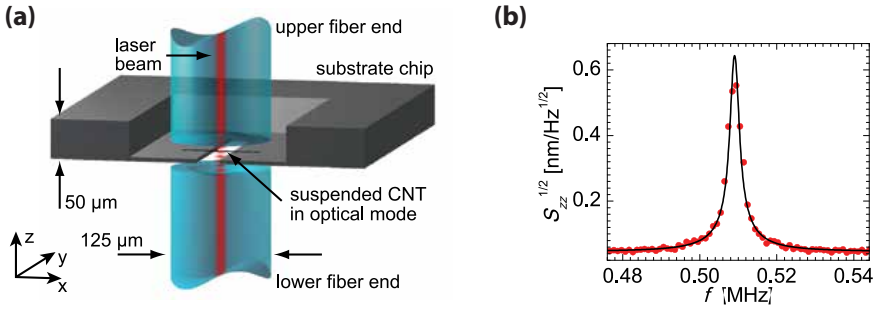

Figure 4.10: Illustration of the experimental setup used by Stapfner *et al.* to resolve the thermal motion of a doubly clamped carbon nanotube resonator [86]. **(a)** Schematic view of cavity and sample chip with the carbon nanotube introduced into the cavity mode. **(b)** Nanotube's thermal noise peak with Lorentzian fit (black) and data points calibrated to Brownian vibrational amplitudes.

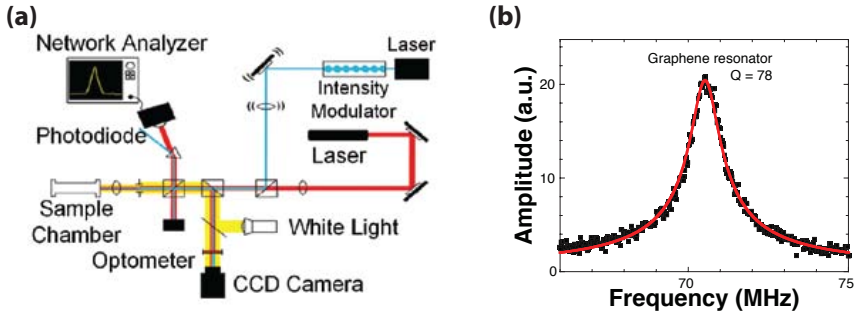

Figure 4.11: Graphene vibrations detection with optical interferometry. **(a)** Schematic of the optical transduction scheme used by Bunch *et al.* to detect the motion of graphene resonators. **(b)** Amplitude versus frequency taken with optical drive for the fundamental mode of the single-layer graphene resonator. A Lorentzian fit of the data is shown in red. Figure adapted by [22].

transduction scheme, the graphene's motion actuation can be done either capacitively, as described in the previous section, or optically. The optical actuation is based on a laser beam which is focused on the membrane with intensity which is modulated on the driving frequency. Due to the photo-thermal effect the graphene is contracting/expanding periodically which leads to a driving force and consequently to its motion. A second laser, that is focused on the graphene, is responsible for its motion detection. The graphene acts as the one end of a low-finesse Fabry-Perot cavity, while the substrate as the other end. As the graphene membrane vibrates it modulates the light intensity that is comes back from the cavity. This light is detected by a fast photo-diode and by recording its output with a signal analyzer, it is possible to spectrally resolve graphene's motion.

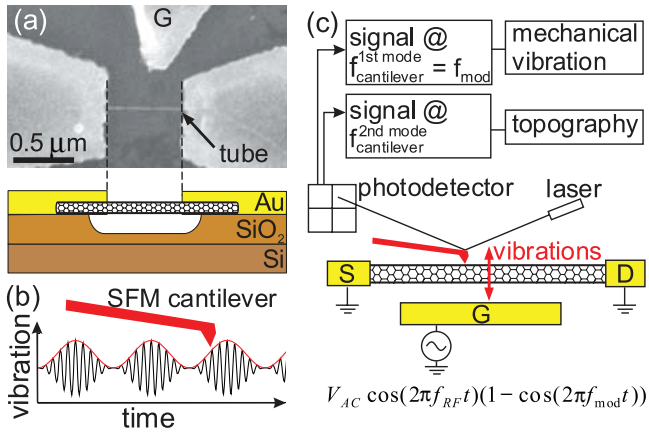

Figure 4.12: Detection of carbon nanotube vibrations using the tip of a scanning force microscope, done by Garcia-Sanchez *et al.* in 2007. Figure adapted from [91].

4.4 Microscopy techniques

Apart from the commonly used electrical and optical transduction schemes, microscopy techniques have also been utilized for the detection of graphene or nanotube mechanical vibrations. For instance, Garcia-Sanchez *et al.* showed that is possible to detect the vibrations of carbon nanotube resonators using Scanning Force Microscopy (SFM) techniques [91] and later on the same was demonstrated for graphene [92]. The principle of operation is illustrated in Figure 4.12. The nanotube (or graphene) is actuated capacitively by applying an oscillating potential at the back gate $V_{\mathrm{AC}}(\omega)$ while the SFM is imaging in tapping mode. When the driving force reaches the resanace frequency of the tube, the detected amplitude from the SFM is maximizing. Because the resonance frequency the SFM cantilever $f_{\mathrm{cantilever}}$ is much lower compared to the nanotube, the applied driving force is 100% modulated. This allows the SFM tip to essentially sense the modulation envelope of the vibrations (Figure 4.12). For increasing the signal the modulations frequency f_{mod} can be set equal to the resonance frequency of the SFM tip.

Another way to detect the vibrations of carbon nanotubes is by using electron microscopy techniques. Treacy *et al.* [93] measured the Young's modulus of carbon by imaging their thermal vibration with a Tunneling Electron Microscope (TEM). The average statistics of their thermally driven motion appears as blurring on the TEM image and increases with temperature (Figure 4.13(a)). In a similar way, Babić *et al.* [94] image the thermal motion of doubly clamped carbon nanotubes using a Scanning Electron Microscope (Figure 4.13(b)).

As we will demonstrate in chapter 6, it is also possibly to resolve the real-time mechanical vibration of carbon nanotube resonators by using a focused electron beam.

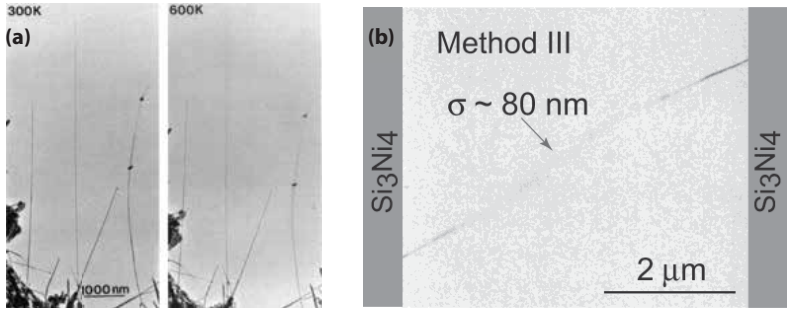

Figure 4.13: Imaging carbon nanotubes thermal vibrations usign electron microscopy techniques. **(a)** Bright-field EM micrographs of free-standing carbon nanotubes shown the blurring at the tips due to the thermal vibration. Figure adapted from [93]. **(b)** Imaging the thermal vibration of a doubly-clamped carbon nanotube using a SEM. Figure adapted from [94].

4.5 Read-out schemes comparison

During this chapter the majority of the available motion transduction techniques for graphene and carbon nanotube resonators were presented. In an effort to qualitatively compare their performance, we can conclude that electrical schemes are primarily suitable for cryogenic temperatures where the electronic noise is much lower and the transconductance of the devices higher. The limitations on the bandwidth of such systems can be overcome by the use of frequency mixing techniques, however, in such a case real-time detection is not possible. High bandwidth measurements can be performed in graphene resonators using localized gates in order to minimize parasitic capacitances, or by coupling their motion to a superconducting cavity.

Optical techniques are more suitable for room temperature detection and in particular for graphene resonators where their surface is large. The optical detection of carbon nanotubes represents a very challenging task due to the relatively small interaction overlap between the optical beam waste and the nanotube. In chapter 6 we overcome this issue by coupling a focused electron beam to their motion. The spot sized of a focused ebeam is in the nanometer range offering significant interaction overlap to the motion of the nanotubes. This detection scheme allowed us to detect the thermal fluctuation of carbon nanotube resonators in real-time. Finally, microscopy techniques are more suitable for imaging the vibration of such systems and extracting information on their spatial averaged statistics and on their eigenmode shapes.